Journal of Rock Mechanics and Geotechnical Engineering 18 (2026) 3760–3778

Contents lists available at ScienceDirect

Journal of Rock Mechanics and Geotechnical Engineering

journal homepage: www.jrmge.cn

Full Length Article

# Impact of joint distribution within hard rock mass on tunnel blasting profile: Numerical simulation and field measurement

Junxin Li [a], Wei Wu [a,b,c], Bingyi Pan [a], Baosheng Dong [d], Hehua Zhu [a,b,c,*]

[a] College of Civil Engineering, Tongji University, Shanghai, 200092, China
[b] Key Laboratory of Geotechnical and Underground Engineering of the Ministry of Education, Tongji University, Shanghai, 200092, China
[c] State Key Laboratory of Disaster Reduction in Civil Engineering, Tongji University, Shanghai, 200092, China
[d] China First Highway Xiamen Engineering Co., Ltd., Xiamen, 361021, China

ARTICLE INFO

*Article history:*
Received 7 January 2025
Received in revised form
6 June 2025
Accepted 11 June 2025
Available online 6 September 2025

*Keywords:*
Joint distribution
Drilling and blasting
Overbreak
Dynamic finite element method
Digital twin

ABSTRACT

In hard rock tunnel excavation, controlling the blasting profile to prevent overbreak and underbreak is critical for safety and cost-effectiveness. Discontinuities such as joints and faults significantly affect the mechanical properties of the rock mass, and their distribution critically influences the blasting outcomes. This study explores the impact of joint distribution on the tunnel blasting profile through field measurements and numerical simulations. Real-time monitoring of the tunnel face was conducted using the digital twin method, capturing both rock discontinuities and blasting profiles. Field results revealed that overbreak tends to occur at joints outside contour boreholes, where the joints lead the blasting profile diverging from the borehole connection line. To quantify this effect, dynamic finite element simulations were conducted to assess the influence of borehole-joint distances ($d = 25$ cm, 50 cm, and 100 cm) and intersecting joint angles ($\alpha = 60°$, 90°, and 120°) on blasting stress wave propagation and rock fracture development. The results demonstrated that joints within the hard rock mass guide and restrain the propagation of blasting stress wave, leading to the formation of a fracture zone induced by the reflected stress wave (the RSW fracture zone). The morphology of the RSW fracture zone closely matched the field blasting profile, validating the numerical simulation results. Furthermore, the borehole-joint distance and the intersecting joint angle were found to govern the extent and geometry of the RSW fracture zone. These findings provide valuable insights for optimizing blasting designs in jointed hard rock masses to control tunnel excavation profiles better.

© 2026 Institute of Rock and Soil Mechanics, Chinese Academy of Sciences. Published by Elsevier B.V. This is an open access article under the CC BY-NC-ND license (http://creativecommons.org/licenses/by-nc-nd/4.0/).

## 1. Introduction

The drilling and blasting method is the most adaptable and cost-effective approach for hard rock fragmentation, and it is widely used in tunnel excavation, mining, hydropower projects, and urban infrastructure development (Zhang et al., 2023). Controlling the blasting profile to minimize overbreak or underbreak is essential for ensuring safety and cost-effectiveness in tunnel construction. The ideal blasting profile follows a smooth line connecting the centers of the contour holes. Overbreak is an undesirable outcome, as it weakens the integrity and stability of the surrounding rock, increasing the risk of rockfalls, spalling, and even tunnel collapse (Hong et al., 2023). Additionally, addressing overbreak requires extra shotcrete and support measures, raising material and labor costs by over 15 % (Zou, 2017a).

Smooth blasting technology is implemented to control overbreak and underbreak in tunnel excavation. One of the key points in smooth blasting is the control of blasting time. Micro-delay blasting control achieves millisecond-level delays between the detonation of adjacent blasting sections. It allows for the staged release of energy and reduces the cumulative shockwave intensity, directing the rock breakage more predictably along the designed profile (Saadatmand Hashemi and Katsabanis, 2020; Sanchidrián et al., 2022). Mechanization plays a vital role in enhancing the quality of tunnel excavation. The jumbo drill rigs equipped with the computerized control system (Wu et al., 2023) have enabled

* Corresponding author. College of Civil Engineering, Tongji University, Shanghai, 200092, China.
*E-mail address:* zhuhehua@tongji.edu.cn (H. Zhu).

Peer review under responsibility of Institute of Rock and Soil Mechanics, Chinese Academy of Sciences.

https://doi.org/10.1016/j.jrmge.2025.06.032
1674-7755/© 2026 Institute of Rock and Soil Mechanics, Chinese Academy of Sciences. Published by Elsevier B.V. This is an open access article under the CC BY-NC-ND license (http://creativecommons.org/licenses/by-nc-nd/4.0/).

centimeter-level accuracy in drilling blasting holes. The precise implementation of the blasting scheme guarantees that the tunnel profile aligns with design expectations. Based on this technology, the drilling and blasting method has reached a relatively mature level (Kumar et al., 2023; Li et al., 2025).

Besides the blasting technology, the blasting outcome is also influenced by the rock mass characteristics (Singh and Xavier, 2005). The engineering properties of rock masses mainly depend on rock discontinuities (Chakraborty et al., 1994) such as joints, faults, and bedding, instead of the properties of the intact rock itself. The discontinuities within the rock mass alter the propagation of blasting stress waves, thereby changing the rock fracture pattern. The blasting profile in layered rock masses is a typical example of discontinuity-controlled tunnel excavation behavior. In Yunnan Province, China, the geological condition is characterized by distinctly reddish-brown mudstone and sandstone with well-developed bedding structures. Due to layered rock masses, angular overbreaks occur at the spandrel on both sides of the tunnel face in several tunnel projects under construction, including the Xiaotianba Tunnel on the Huize-Qiaojia Expressway, as well as the Heijing and Daxiangshu Tunnels on the Muding-Yuanmou Expressway. The occurrence of over-excavation not only leads to a substantial increase in tunnel construction costs but also affects construction quality and safety. To reduce the influence of discontinuity on the rock blasting profile, the pre-split blasting technique (Zhang et al., 2022; Tahir et al., 2023) is employed. The pre-split plane is formed by drilling a row of closely spaced boreholes with small amounts of explosives around the tunnel profile. The subsequent main blast fractures the inner rock mass without damaging the pre-split plane. This technology concentrates the explosive energy, reducing the impact of joints on the rock blasting process, and guides the direction of the rock fracture through the pre-fracture plane around the contour holes. These adjustments help mitigate the influence of discontinuity on the blasting process.

However, the mechanism of significant joints induced over-break in hard rock mass under the tunnel excavation is not sufficiently explored. Different joint distributions like parallel joints, intersecting joints, and single joints lead to varying blasting results (Barton et al., 1974). The influence of the relative positions of the joints and boreholes on the blasting profile requires further investigation. While the impact of joint distribution on tunnel blasting profiles remains underexplored, the influence of joints on rock dynamic response has been extensively studied. Previous research has examined the behavior of the defective rock under dynamic loads (Vazaios et al., 2019) based on different analysis methods:

Laboratory tests provide a controlled environment for the precise discontinuity contribution and multifaceted data monitoring (Tian et al., 2024). The three-dimensional (3D) models with different open joint dip angles can be created using a 3D printer (Wang et al., 2024). The crack distribution and damage characteristics recorded by the X-ray CT scanner show that the open joint changes the crack distribution and induces radial cracks and wing cracks. To record the crack and wave propagation simultaneously, polymethyl methacrylate (PMMA) is used to model the jointed rock mass (Yang et al., 2016; Ma et al., 2023; Liang et al., 2024), which is a rock-like brittle material with high transmittance. The results indicate that stress waves undergo reflection and diffraction at the joint interface, and wing cracks develop at the joint tip. Cause of the sample size affects the laboratory test to fully reflect the field condition, and monitoring the dynamic changes at the moment of blasting is highly challenging.

Numerical methods can better reflect the impact of discontinuities on the blasting behavior of rock mass in real tunnel construction and track the blasting process (Wang et al., 2022; Ling et al., 2023; Lyu et al., 2023). Ma and An (2008) explored the impact of the open joint plane on the blasting-induced rock fractures of a single hole based on the Johnson-Holmquist (J-H) material model and found that the open joint acts like a free face, which reflected the stress wave. Zhu et al. (2007) extensively investigated the influence of various joints on blasting-induced rock fractures and found that for filling-type joints the cracks passing through the joint plane decrease as the joint width increases, and for the open joint (with air as the filling material) the transmitted wave is further reduced and no cracks behind propagate the joint plane.

Besides analyzing the effects of joints on rock blasting, accurate field measurement of joint distribution is also crucial for controlling the blasting profile in jointed rock mass. Xue et al. (2023) proposed a spatial-aware recurrent neural network to predict fracture maps during tunnel excavation based on statistical analysis. Because the joint distribution changes with the tunnel excavation continually, real-time monitoring of the tunnel face to capture both the distribution of rock discontinuities and the blasting profile is essential. Due to the harsh tunnel construction environment, the timely and continuous acquisition of tunnel face information is particularly important. To address it, Qin et al. (2023) developed a robot equipped with a 3D laser scanner capable of non-contact, computer vision-based detection of rock joints, thereby reducing the risks associated with manual data collection. With the development of information technology, real-time data transmission from the field enables the establishment of a digital model that accurately reflects on-site conditions. This method, known as the digital twin, facilitates dynamic monitoring of tunnel faces throughout the construction process (Ye et al., 2023; Fang et al., 2024).

To investigate the impact of joint distribution within the hard rock mass on the tunnel blasting profile, the real-time field measurement was conducted using the digital twin method to capture the excavation profile and the joint distribution, while the dynamic finite element method (DFEM) was applied to simulate the dynamic response of the jointed rock mass.

## 2. Engineering background

### 2.1. Site description

This study relies on the Yinggeling Highway Tunnel, currently under construction in the central mountainous area of Hainan Province, China. The tunnel is 8.2 km long, with a general northwest-southeast alignment and a maximum burial depth of 338 m. The stratigraphy of the project area primarily consists of Quaternary artificial fill, alluvial sand and pebble, slope residual debris, Cretaceous sandstone, conglomerate, and Permian-Triassic granite.

Based on on-site hydrogeological surveys, drilling data, and field tests, groundwater at the tunnel site is primarily hosted in Quaternary gravelly soils, highly weathered rock, and fault zones. In contrast, slightly weathered rock strata contain only minimal water and exhibit poor permeability. Fault zones present a high risk of water inrush, while the risk of water surges during tunnel excavation in other segments is low.

The local longitudinal section of the Yinggeling Tunnel, spanning from ZK11 + 000 to ZK12 + 000, is shown in Fig. 1. Through the on-site survey, geophysical interpretation, and drilling data, these sections consist of Permian-Triassic granite, appearing in gray, gray-white, or flesh-red colors, with a coarse-grained structure and blocky texture. During tunnel excavation, no water inrush, seepage, or sudden surges were observed from ZK11 + 900 to the ZK11 + 600 section.

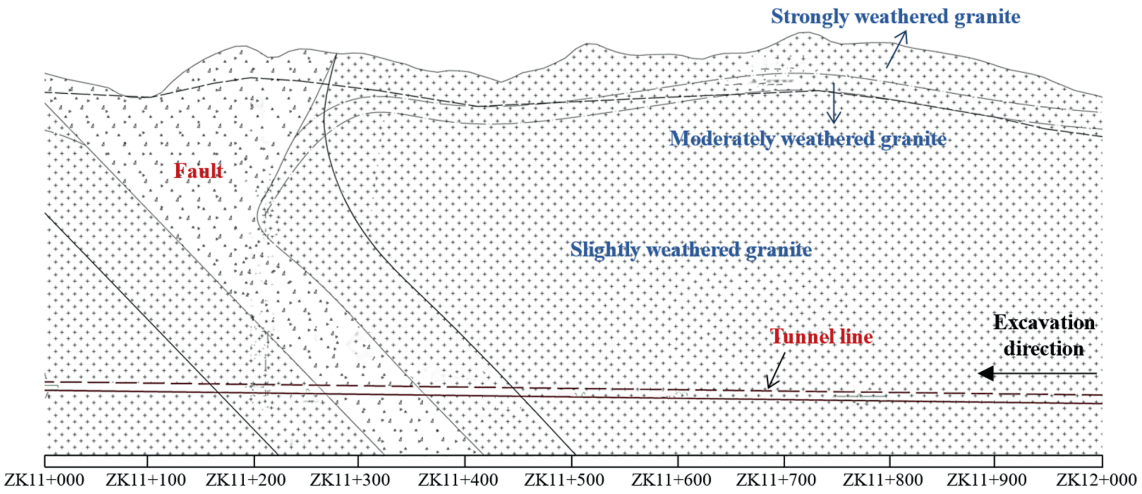



**Fig. 1.** Longitudinal Section of the Yinggeling Tunnel from ZK11 + 000 to ZK12 + 000. Note: ZKxx + yyy indicates a point at a chainage of xx km and yyy m from the entrance of the tunnel on the left line.

The surrounding rock is stable, with resistance to collapse or spalling following excavation. Geological parameters and drilling results from the on-site geological survey of the Yinggeling Tunnel are summarized in Table 1.

### 2.2. Blasting design

According to the geological environment, the full-face tunnel excavation is adopted using the drilling and blasting method. The tunnel blasting design is shown in Fig. 2.

Smooth blasting technology is employed to ensure that the tunnel blasting outcomes align with the design profile. From the inside to the outside, it consists of cut holes (shown in red), stopping holes (shown in yellow), lifter holes (shown in blue), and contour holes (shown in black). Blasting holes are linked with detonating cords, following the order from MS0 to MS5, with a time interval of 100 ms between each detonation. A proper delay time can enhance rock blasting efficiency.

Cut holes are drilled at a large inclination and initiated first to create a blast cavity at the center of the tunnel face. The blast cavity increases the free surface and improves the efficiency of subsequent blasts. Stopping holes, drilled at a small inclination, compress the surrounding rock toward the blast cavity, further expanding it. Lifter and contour holes are drilled vertically. Contour holes are arranged along the tunnel design profile with small spacing and employ decoupled charging with minimal explosives to precisely control the tunnel blasting profile. Functionally, cut holes play a critical role in initiating successful rock breakage, while contour holes determine the final shape of the tunnel blasting profile.

**Table 1**
Test results of sonic logging and drilling samples at the borehole located 20 m to the right of ZK11 + 842 in the Yinggeling Tunnel.

| Parameter | Value |
|---|---|
| In situ bulk density (N/ $m^3$) | $2.68 \times 10^4$ |
| P-wave velocity (m /s) | 3824 |
| Dynamic Poisson's ratio | 0.32 |
| Integrity coefficient, $K_v$ | 0.66 |
| Dynamic elastic modulus (Pa) | $2.142 \times 10^{10}$ |
| Dynamic elastic shear modulus (Pa) | $8.76 \times 10^9$ |
| Dry compressive strength (Pa) | $6.48 \times 10^7$ |

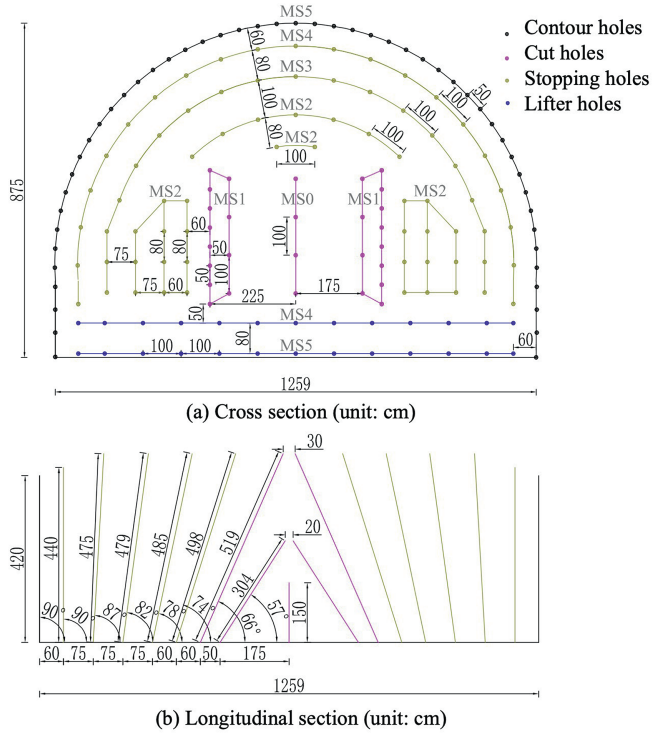
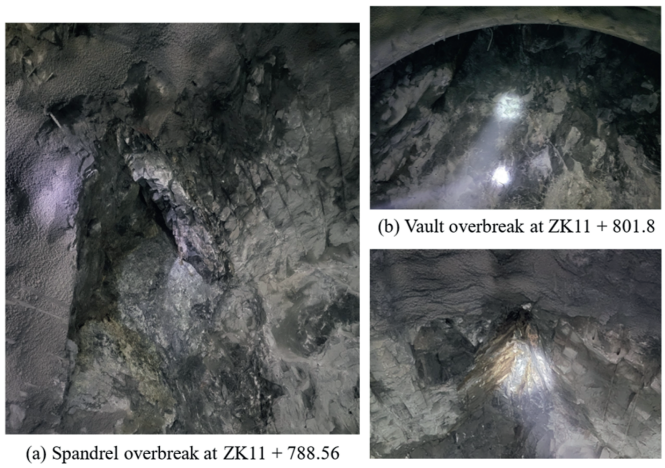



**Fig. 2.** Tunnel blasting design of the Yinggeling Tunnel.

### 2.3. Engineering problem

Smooth blasting technology was highly effective, keeping overbreak within 20 cm. However, from ZK11 + 788 to ZK11 + 825, several overbreaks occurred, with the deepest exceeding 200 cm, well beyond the control standard, as shown in Fig. 3. According to the on-site overbreak situation, the smooth surfaces could be structural planes in the rock mass, which indicates that the severe overbreak is likely caused by those significant discontinuities within the rock mass.

To investigate the impact of joint distribution on the tunnel blasting profile in hard rock mass, a combination of numerical simulation and field measurement was employed. The numerical



(a) Spandrel overbreak at ZK11 + 788.56

(b) Vault overbreak at ZK11 + 801.8

(c) Vault overbreak at ZK11 + 824.8

**Fig. 3.** The overbreak sections in the Yinggeling tunnel construction: (a) Spandrel overbreak at ZK11 + 788.56; (b) Vault overbreak at ZK11 + 801.8; and (c) Vault overbreak at ZK11 + 824.8.

simulation analyzed rock blasting performance in different joint distributions. The field measurement, using the digital twin method, was conducted to monitor the tunnel excavation face in real time, providing the joint distribution and the tunnel blasting profile.

## 3. Numerical simulation method

This section introduces the numerical simulation method used in this study, including the rock constitutive model, the explosive model, and the parameter calibration method. Compared to field and laboratory testing, the numerical simulation method is cost-effective and flexible for analyzing various experimental schemes.

Studies on the dynamic mechanism of rock blasting (Zou, 2017b) show that rock fragmentation is caused by the combined effects of explosive shock waves and detonation gases. During the rapid blasting process, the impact force can reach 1 GPa–10 GPa, which is a high-strain and large-deformation problem and involves fluid-solid coupling between the rock mass and the explosive gas.

Various numerical methods have been developed to simulate rock blasting and fracture processes, each with its own advantages and limitations (Cai and Yan, 2024; Wang et al., 2025; Wang and Yin, 2025). The discrete element method (DEM) can simulate crack propagation by defining the contact between particles (Potyondy and Cundall, 2004; Lisjak and Grasselli, 2014). However, for continuous media, like intact rock, contact parameters remain challenging due to the lack of direct experimental calibration. The finite difference method (FDM) has high computational efficiency (Zuazua, 2005; Fornberg and Flyer, 2015). However, it exhibits limited capability in handling complex geometries, such as cracks and irregular boundaries. In contrast, the dynamic finite element method (DFEM) is well-suited for nonlinear material analysis and integrates mature fluid-solid coupling algorithms for blasting dynamic simulation (Wang et al., 2015, 2025; Liu et al., 2022).

Comparing several numerical simulation methods, the DFEM is employed to simulate both the blasting process and the impact-induced damage in the rock mass. The Arbitrary Lagrange-Euler (ALE) coupling algorithm (Donea et al., 2004) is applied, which is particularly well-suited for addressing fluid-solid coupling and highly nonlinear material behaviors. ALE provides accurate modeling of shock wave propagation and impact-induced damage between the fluid (high-pressure gas and air) and solid (rock). Its flexible meshing and material tracking mechanisms ensure numerical stability throughout the later stages of the explosion process. The detailed modeling process will be presented in Section 4.2.

### 3.1. Rock constitutive model

The Holmquist-Johnson-Cook (HJC) constitutive model (Holmquist et al., 1993), proposed by Holmquist, Johnson, and Cook, is widely used in rock blasting simulations. It effectively describes the behavior of brittle concrete or rock materials under conditions of large strain, high strain rates, and high pressures. The HJC model consists of three parts: the strength equation (the yield surface equation), the fracture damage evolution equation, and the equation of state. Those equations involve 5 strength parameters, 3 damage parameters, 7 equations of state parameters, and 4 basic physical parameters, totaling 19 parameters. The related schematic illustration is shown in Fig. 4.

The strength equation is given as

$$\sigma^* = \left[A(1-D) + BP^{*N}\right](1 + C\ln\dot{\varepsilon}^*) \tag{1}$$

where $\sigma^* = \sigma/f_c'$ is the normalized effective stress (where $\sigma$ is the actual effective stress shown in Eq. (13) and $f_c'$ is the quasi-static uniaxial compressive strength), $D(0 \le D \le 1)$ is damage shown in Eq. (2), $P^* = P/f_c'$ is the normalized pressure (where $P$ is the actual pressure shown in Eq. (14), $\dot{\varepsilon}^* = \dot{\varepsilon}/\dot{\varepsilon}_0$ is the dimensionless strain rate (where $\dot{\varepsilon}$ is the actual strain rate and $\dot{\varepsilon}_0 = 1\ \mathrm{s}^{-1}$ is the reference strain rate), and $A, B, C$ and $N$ are the material constants. $A$ is the normalized cohesive strength, $B$ is the normalized pressure hardening coefficient, $C$ is the strain rate coefficient, and $N$ is the pressure hardening exponent, the calibration method for which is described in Section 3.3. $S_{\max}$ is defined as the maximum normalized effective stress that the material can reach.

The fracture damage evolution equation is given as

$$D = \sum \frac{\Delta\varepsilon_p + \Delta\mu_p}{\varepsilon_p^f + \mu_p^f} \tag{2}$$

where $\Delta\varepsilon_p$ is the equivalent plastic strain during a cycle of integration, $\Delta\mu_p$ is the plastic volumetric strain during a cycle of integration, and $\varepsilon_p^f + \mu_p^f = f(P)$ is the plastic strain to fracture under a constant pressure $P$ (where $\varepsilon_p^f$ is equivalent plastic strain at fracture and $\mu_p^f$ is the plastic volumetric strain at fracture) and expressed as

$$\varepsilon_p^f + \mu_p^f = D_1(P^* + T^*)^{D_2} \ge EF_{\min} \tag{3}$$

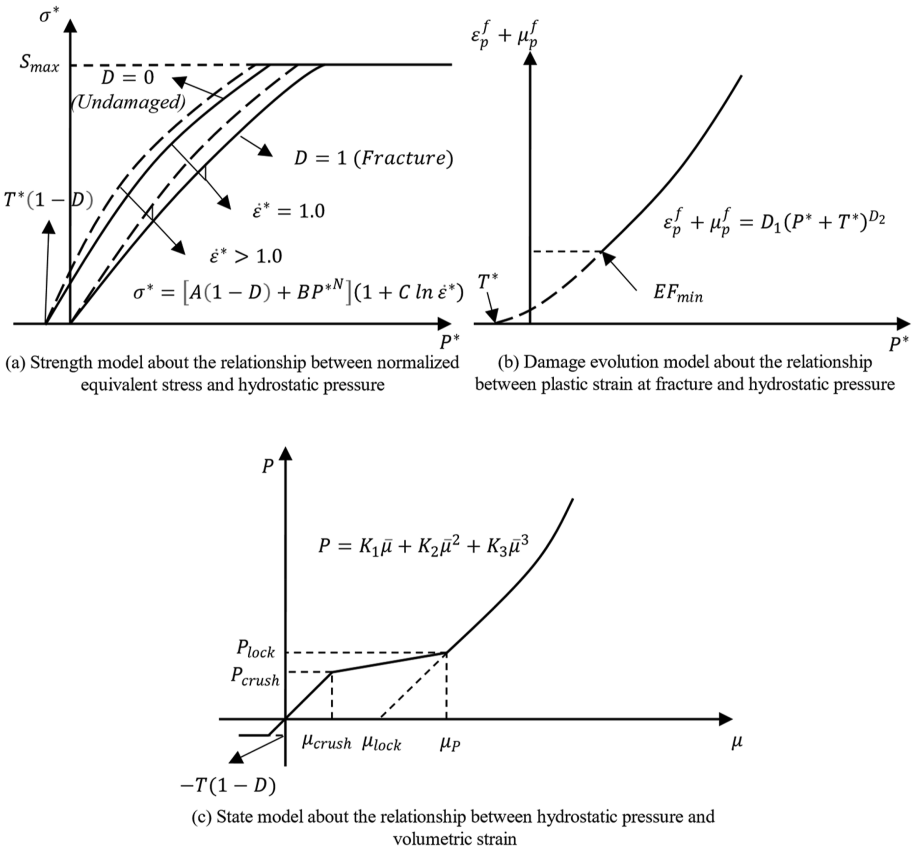
where $D_1$ and $D_2$ are the constants, $T^* = T/f_c'$ is the normalized tensile strength (where $T$ is the maximum tensile hydrostatic pressure that the material can withstand), and $EF_{\min}$ is defined as the minimum plastic strain leading to material fracture.

The equation of state describes the relationship between hydrostatic pressure and volumetric strain, divided into three phases.

Firstly, the linear elastic phase occurs at $-T(1-D) \le P < P_{\mathrm{crush}}$ and is given as

$$P = K_e\mu \tag{4}$$

where $P_{\mathrm{crush}}$ is the pressure at which air voids are gradually compressed out of the material, $K_e$ is the elastic bulk modulus, and $\mu = \frac{\rho}{\rho_0} - 1$ is the volumetric strain, which is less than $\mu_{\mathrm{crush}}$ (where




(a) Strength model about the relationship between normalized equivalent stress and hydrostatic pressure

(b) Damage evolution model about the relationship between plastic strain at fracture and hydrostatic pressure

(c) State model about the relationship between hydrostatic pressure and volumetric strain

**Fig. 4.** Schematic illustration of Holmquist-Johnson-Cook (HJC) material model.

$\rho_0$ is initial density, $\rho$ is current density, and $\mu_{\text{crush}}$ is the volume strain corresponding to $P_{\text{crush}}$).

Secondly, the plasticity phase occurs at $P_{\text{crush}} \le P < P_{\text{lock}}$ and is given as

$$P = K_{\text{p}}(\mu - \mu_{\text{crush}}) + P_{\text{crush}} \tag{5}$$

where $P_{\text{lock}}$ is the pressure at fully dense material, $K_{\text{p}} = \frac{P_{\text{lock}} - P_{\text{crush}}}{\mu_{\text{P}} - \mu_{\text{cruch}}}$, and $\mu_{\text{crush}} < \mu \le \mu_{\text{P}}$ (where $\mu_{\text{p}}$ is the volume strain corresponding to $P_{\text{lock}}$ and $\mu_{\text{lock}} = \frac{\rho_{\text{grain}}}{\rho_0} - 1$ is the locking volumetric strain, with $\rho_{\text{grain}}$ representing the grain density).

Thirdly, the dense phase occurs at $P \ge P_{\text{lock}}$, for the loading process is given as

$$P = K_1\bar{\mu} + K_2\bar{\mu}^2 + K_3\bar{\mu}^3 \tag{6}$$

and for the unloading process is given as

$$P = K_1\bar{\mu} \tag{7}$$

where $K_1, K_2$ and $K_3$ is the pressure constants and $\bar{\mu} = \frac{\mu - \mu_{\text{lock}}}{1 + \mu_{\text{lock}}}$ is the modified volumetric strain (where $\mu > \mu_{\text{lock}}$).

### 3.2. Explosive and air model

Type 2 emulsion explosive charge is used in this tunnel excavation, and the parameters of explosive properties are shown in Table 2. The Jones-Wilkins-Lee (JWL) equation of state (EOS) (Menikoff, 2015) can be used to model the detonation of an explosive charge, which is expressed as

**Table 2**
Parameters of Type 2 emulsion explosives.

| Parameter | Value |
|---|---|
| Density, $\rho_{0_expolisve}$ (kg /m$^3$) | 1.3 |
| Detonation velocity, $D_{\text{explosive}}$ (m /s) | 4000 |
| Detonation pressure, $P_{\text{E_D}}$ (Pa) | $3.362 \times 10^9$ |
| Internal energy, $E_{\text{J}}$ (Pa) | $8.56 \times 10^9$ |
| $A_{\text{J}}$ (Pa) | $6.253 \times 10^{11}$ |
| $B_{\text{J}}$ (Pa) | $2.329 \times 10^{10}$ |
| $R_1$ | 5.25 |
| $R_2$ | 1.6 |
| $\omega$ | 0.28 |

$$P_{\text{J}} = A_{\text{J}}\left(1 - \frac{\omega}{R_1 V}\right)\mathrm{e}^{R_1 V} + B_{\text{J}}\left(1 - \frac{\omega}{R_2 V}\right)\mathrm{e}^{R_2 V} + \frac{\omega E_{\text{J}}}{V} \tag{8}$$

where $V$ and $E_{\text{J}}$ are the relative volume and internal energy, respectively. $A_{\text{J}}$, $B_{\text{J}}$, $R_1$, $R_2$, and $\omega$ are material constants.

The Gamma Law equation of state is an important model for describing gas behavior, particularly in high-pressure, rapidly dynamic processes such as explosions and shock wave propagation. Combining a linear polynomial equation with the Gamma Law equation, a simpler model can be established for simulating air material:

$$P_{\text{Air}} = (C_4 + C_5\mu_{\text{Air}})E_{\text{A}} \tag{9}$$

where $\mu_{\text{Air}} = \frac{\rho_{\text{Air}}}{\rho_{0_\text{air}}}$ is the air volumetric strain, and $\frac{\rho_{\text{Air}}}{\rho_{0_\text{air}}}$ is the ratio of current density to reference density. $E_{\text{A}}$ is the internal energy

per unit reference volume.

The value of parameters for JWL EOS and air material based on data from the literature (Tawadrous, 2011) are shown in Tables 2 and 3 separately.

### 3.3. Parameter calibration

The rock fragments generated during tunnel blasting are too small to provide enough rock samples for dynamic impact testing. The following presents a method for determining the HJC parameters, ensuring they align with the field rock conditions and simplify the calibration process.

The strength model is shown in Fig. 4a. The values of $\rho, f_c'$ and $G$ are given in geological survey reports and field test results as shown in Table 1. The value of $K_e$ can be calculated using the shear modulus and the elastic modulus provided in the geological survey report. Due to the lack of impact test results for on-site rock specimens, the strain rate parameter $C$ is adopted from the literature (Wen et al., 2016), with $C = 0.0013$.

The Hoek-Brown criterion is a widely used empirical relationship that describes the strength of rock materials, which is expressed as

$$\sigma_1 = \sigma_3 + f_c'\left(m_i\frac{\sigma_3}{f_c'} + s\right)^a \tag{10}$$

when $\sigma_1 = 0$, the tensile strength of good quality rock can be written as

$$T = \frac{f_c'}{2}\left(-m_i + \sqrt{m_i{}^2 + 4s}\right) \tag{11}$$

For the intact granite, the parameters are $s = 1, a = 0.5, m_i = 30,$ and the tensile strength is $T = 2.2 \times 10^6$ Pa.

Ignoring the strain rate and damage effect, the strength equation of the HJC model is

$$\sigma^* = A + BP^{*N} \tag{12}$$

Using the three principal stresses, $\sigma_1$, $\sigma_2$, and $\sigma_3$, the effective stress $\sigma$ has the form of

$$\sigma = \frac{1}{\sqrt{2}}\sqrt{(\sigma_1-\sigma_2)^2 + (\sigma_2-\sigma_3)^2 + (\sigma_3-\sigma_1)^2} \tag{13}$$

and the pressure $P$ has the form of

$$P = \frac{\sigma_1 + \sigma_2 + \sigma_3}{3} \tag{14}$$

A series of $\sigma_1$ and $\sigma_3$ can be obtained from Eq. (10), and $\sigma^*$ and $P^*$ can be calculated using Eqs. (13) and (14). $A = 0.285, B = 2.193,$ $N = 0.828$ are then obtained by curve-fitting using Eq. (12), and the fitting curve is shown in Fig. 5a.

The fracture damage model is shown in Fig. 4b. The damage parameter $D_1 = 0.05$ is calculated using Eq. (15) and $D_2 = 1$,

**Table 3**
Parameters of air material.

| Parameter | Value |
|---|---|
| Density, $\rho_{0_air}$ (kg /m$^3$) | 0.0012 |
| Initial internal energy per unit Reference volume, $E_{A0}$ (Pa) | $2.5 \times 10^5$ |
| $C_4$ | 0.4 |
| $C_5$ | 0.4 |

$$D_1 = \frac{0.01}{\left(\frac{1}{6} + T^*\right)} \tag{15}$$

The equation of state model is shown in Fig. 4c. $P_{crush}$ and $\mu_{crush}$, can be given by $P_{crush} = f_c'/3$ and $\mu_{crush} = P_{crush}/K_e$. Assuming the porosity of the rock is 1.2 %, when the rock is completely crushed, the locking volumetric strain $\mu_{lock}$ is 0.0121.

The Hugoniot relation is a physical equation that describes the behavior of a material under conditions of high pressure and temperature, particularly during the influence of a shock wave or explosion, which is expressed as

$$P = C_H{}^2\rho_0\mu(\mu+1)\Big/[(1-S)\mu+1]^2 \tag{16}$$

For granite, the impact compression constants are determined as $C_H = 2100$ and $S = 1.68$. A series value of $(P, \mu)$ can be given by Eq. (16). $K_1 = 16.2$, $K_2 = 1.5$, and $K_3 = 115.9$ are obtained by polynomial fitting, which is shown in Fig. 5b, and $P_{lock} = 1.2 \times 10^9$ Pa.

The HJC parameters of rock mass in the Yinggeling Tunnel at ZK11 + 842 are shown in Table 4.

## 4. Field measurement and simulation scheme

### 4.1. Digital twin method

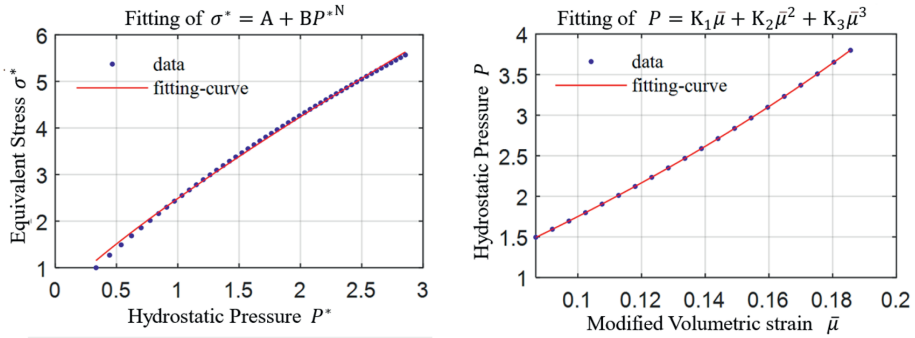
Our research team has developed a rapid field measurement system using the digital twin method to collect and recognize tunnel face information. Building a digital twin model offers a safer and more efficient way to obtain tunnel face information compared to traditional methods such as manual sketching and total station measurement. The following outlines the tunnel face measurement process using the digital twin method:

First, data for the digital twin model building is multi-view images of the tunnel face captured by a smartphone or camera. To ensure the successful reconstruction of the tunnel face model, image acquisition should be conducted after excavation dust has settled, thereby minimizing visual interference. Uniform lighting without significant color temperature variations should be used from both sides to evenly illuminate the tunnel face. For completeness of the reconstructed model, capture at least three images of the tunnel face from each of over three different positions. The image collection positions are shown in Fig. 6a.

Second, a 3D point cloud model of the tunnel face is reconstructed using the image sequence based on virtual multi-view stereo imaging techniques. The 3D point cloud model reconstructed from the image sequence is compared with the point cloud model obtained using a millimeter-level laser scanner. Iterative Closest Point (ICP) matching was performed between the two models, yielding a nearest point distance of less than 2 cm and a root mean square error (RMS) of 0.04. These results indicate that the reconstructed model demonstrates high accuracy. The 3D reconstruction point cloud model of the tunnel face is shown in Fig. 6b.

Third, automatic identification of rock mass characteristics is performed on the reconstructed 3D point cloud. An improved density-based spatial clustering of applications with noise (DBSCAN) algorithm (Chen et al., 2017; Zhang et al., 2024) is employed for the automatic identification and grouping of rock discontinuities, while an optimized k-means++ clustering method (Zhang et al., 2020) is used for the optimal segmentation of trace lines.

Finally, a cloud-based platform is established using cloud




(a) Fitting of strength parameters (b) Fitting of the equation of state parameters

**Fig. 5.** Curve-fitting for HJC model constants.

**Table 4**
The HJC parameters of rock mass in the Yinggeling Tunnel at ZK11 + 842.

| Parameter | Value |
|---|---|
| Density, $\rho_0$ (kg /m$^3$) | 2680 |
| Bulk modulus, $K_e$ | 12.87 |
| Uniaxial compressive strength, $f_c'$ (Pa) | 6.48 × 10$^7$ |
| Tensile strength, $T$ (Pa) | 2.2 × 10$^6$ |
| $A$ | 0.285 |
| $B$ | 2.193 |
| $N$ | 0.828 |
| $C$ | 0.0013 |
| $S_{max}$ | 5.5 |
| $EF_{min}$ | 0.01 |
| $D_1$ | 0.1 |
| $D_2$ | 1 |
| $P_{crush}$ (Pa) | 2.16 × 10$^7$ |
| $\mu_{crush}$ | 0.0017 |
| $P_{lock}$ (Pa) | 1.2 × 10$^9$ |
| $\mu_{lock}$ | 0.0121 |
| $K_1$ (Pa) | 1.62 × 10$^{10}$ |
| $K_2$ (Pa) | 1.5 × 10$^9$ |
| $K_3$ (Pa) | 1.159 × 10$^{11}$ |

computing technology (Zhu et al., 2017; Li et al., 2019). By uploading image data, automated computational analysis is performed remotely, enabling continuous modeling of the newly exposed tunnel face. The identification results of rock mass characteristics are then transmitted back in real-time, establishing a continuously updated digital twin model.

The entire operation process takes approximately 10–15 min. Tunnel face information is collected through photography, and geologists do not need to stay in front of unsupported surrounding rock for a long time. Data collection is between the "slag removal" and "spraying concrete support" processes, avoiding the interruption of construction. The cloud platform allows for the rapid transmission of data, generation of the point cloud tunnel face model, analysis of rock mass information, and feedback of results within 3–5 min. The generated digital twin model (the point cloud tunnel face model) can be accessed via the cloud-based platform by individuals who are unable to be on-site.

The ZK11 + 813 section is chosen to illustrate the process of the field measurement, as shown in Fig. 6. The point cloud model (Fig. 6b) was generated from image sequences of the tunnel face (Fig. 6a), which were captured by a camera or smartphone in different positions. The overbreak was observed on the upper left side of the tunnel face, characterized by a set of intersecting planes with a depth of about 2 m (Fig. 6c). The distribution of the rock mass traces is identified on the point cloud model using a clustering algorithm (Zhang et al., 2020, 2024). The overbreak profile is triangular, and the edges were parallel to the main directions of the rock trace lines (Fig. 6d).

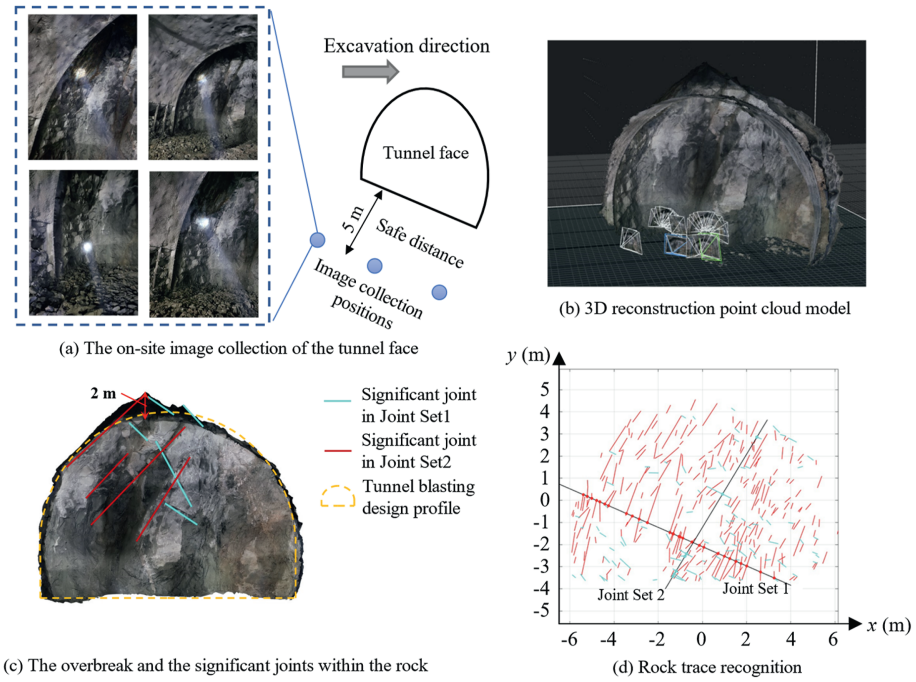
During the long-term monitoring, several overbreak sections occurred in the section from ZK11 + 788 to ZK11 + 825. These overbreak sections exhibited similar characteristics, with joints present on the outer side of the contour boreholes. It was inferred that the overbreak surfaces corresponded to pre-existing joints located on the outer side of the contour boreholes. The interaction between these joints and adjacent boreholes affected the propagation of blasting stress waves, leading to the overbreak. The following section will quantitatively investigate the impact of joint distribution on stress wave propagation and fracture mode in rock blasting using the DFEM.

### 4.2. Scheme design

To enhance computational efficiency, both localized and full-scale models were employed in the simulation. Specifically, the localized models were used to investigate how the distance between joints and boreholes, as well as the angle of intersecting joints, influences blasting-induced crack propagation. Based on the insights from the localized analysis, a typical tunnel excavation section was selected for full-scale tunnel blasting simulation. The results were compared with field measurements to validate the accuracy and effectiveness of the proposed numerical simulation method.

The borehole has a diameter of 4.5 cm, with a charge diameter of 3.2 cm, and the borehole length ranges from 1.5 m to 5 m. Since the charge length is significantly greater than the borehole diameter and the drilling inclination is neglected, a plane strain model is adopted to simulate the explosive process.

The boundary conditions and model size have a large impact on the results. Preliminary tests were conducted to assess the influence. Single-hole blast models were simulated for two boundary conditions (non-reflecting boundary and free boundary) and different model sizes (50 cm, 100 cm, 200 cm, and 400 cm), as




(a) The on-site image collection of the tunnel face

(b) 3D reconstruction point cloud model

(c) The overbreak and the significant joints within the rock

(d) Rock trace recognition

**Fig. 6.** Digital twin model of the tunnel face constructed from on-site images at section ZK11 + 813.

shown in Fig. 7. Under free boundary condition, blasting-induced stress waves reflect at the model boundaries, causing layer cracks in the rock mass, as shown in Fig. 7b, i. Since the effect of blasting does not reach the mountain boundaries during tunnel excavation, non-reflecting boundary conditions better represent the actual situation, as shown in Fig. 7a, i. Comparing the results with different model sizes, as shown in Fig. 7c, i-iii, the rock length was set to 200 cm to ensure both the representation of the blast influence and improved computational efficiency.

The blasting results are also influenced by the direction of stress wave propagation and joint size. Field observations show that the joints have a minimal opening angle and no inclusions, making the unfilled joint model a more accurate representation of the actual conditions. As shown in Fig. 8a, when the blasting stress wave propagates parallel to the joint plane, the surrounding rock fractures along the joint. At a 45° oblique incidence, the rock mass between the blast hole and the joint becomes more fragmented. When the stress wave strikes the joint perpendicularly, the area of rock fragmentation between the joint and the blasting hole is even greater. Under perpendicular incidence of blasting stress waves on the joint interface, the rock fracture patterns were compared for three different joint lengths. The results, as shown in Fig. 8b, indicate that with long joints, the extent and area of rock fragmentation between the blasting hole and the joint are the greatest.

Based on the preliminary test results, the long unfilled joint, with the stress wave perpendicular to the joint interface, was selected to maximally represent the impact of the joint on rock blasting. For localized models, the rock model is represented by a rectangular blue block with dimensions of 200 cm × 200 cm (length × width), and non-reflecting boundaries were applied around the model to simulate an infinitely large rock mass region. The joints were set as unfilled discontinuities with dimensions 120 cm × 0.5 cm (length × width). The distances between the borehole and the joint are set as 25 cm, 50 cm, and 100 cm, as shown in Fig. 9a. Additionally, the angles of the intersecting joint are set as acute angles, right angles, and obtuse angles ($\alpha = 30°$, 60°, and 120°) as shown in Fig. 9b. For full-scale tunnel blasting models, the size of the rock model is 1911 cm × 1288 cm (length × width) with a non-reflecting boundary condition. The positions of blasting holes follow the blasting design introduced in Section 2.2. The tunnel blasting model without joints is shown in Fig. 9c. The tunnel blasting model with an intersecting joint is shown in Fig. 9d, and the two joints have the sizes of 623 cm × 0.5 cm (length × width) and 665 cm × 0.5 cm (length × width), respectively.

The air material was modeled using the Eulerian element, the explosive was represented with the volume fraction method (Yao et al., 2017), and the rock was modeled using the Lagrange element. The eight-node hexahedral element is meshed to ensure the accuracy and efficiency of the DFEM simulation results. Compared to the four-node tetrahedral element, the eight-node hexahedral element has more nodes and provides higher computational accuracy. Additionally, for the same model, the hexahedral element results in fewer elements and shorter computation time. To reduce the stress wave distortion and show the process of rock fracture, the size of the element is from 0.128 cm to 1 cm. As shown in Fig. 10, the local mesh around the charge was set as 0.128 cm for greater precision, and the mesh farther from the borehole was set as 1 cm to reduce computational time.

## 5. Results and analysis

The joint affects the propagation of blasting waves and the development of cracks in the rock mass. The following explains the numerical simulation results and the comparison between full-scale tunnel simulation and field measurements.

### 5.1. Influence of the borehole-joint distance

Extensive research on single-borehole rock blasting without joints has shown that the dynamic response and rock fracture are typically divided into three stages (Dehghan Banadaki and Mohanty, 2012; Ma et al., 2023): First, the shock wave generated by the explosion, with high temperature and high pressure,

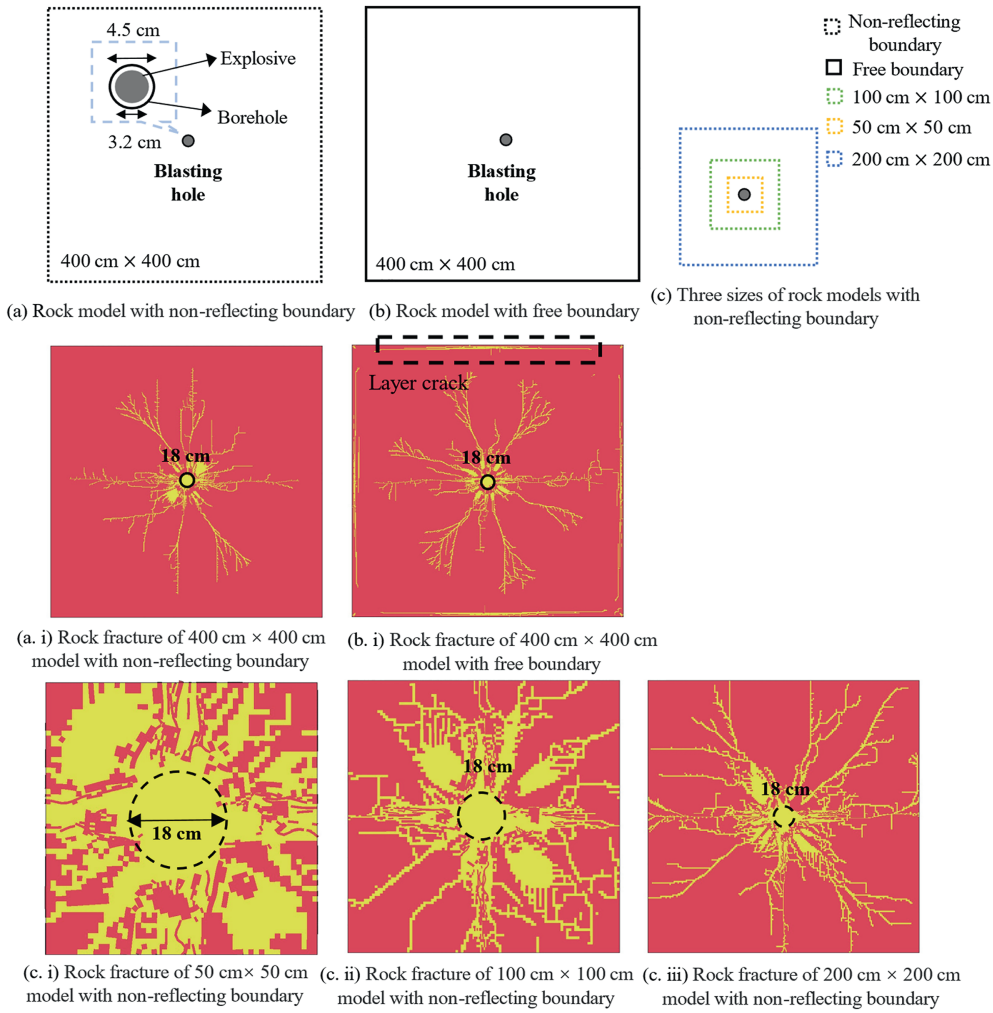



**Fig. 7.** The influence of model size and boundary conditions on the results. Note: The rock model size is given as $a \times b$, where $a$ is the length and $b$ is the width (e.g. 400 cm × 400 cm). The area of the crushed zone is marked by black dashed circle, and the diameter is labeled.

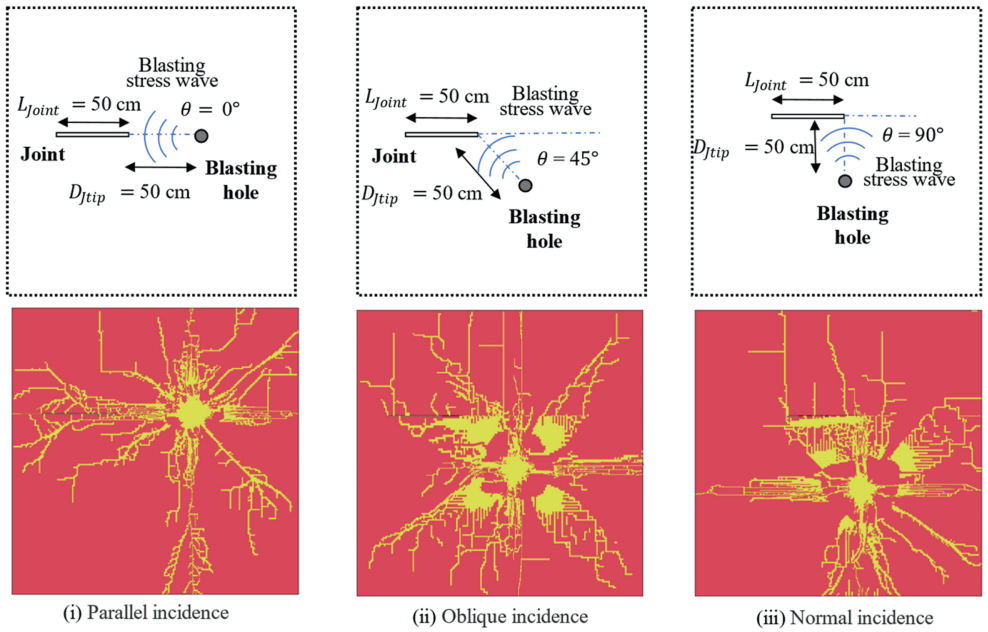
propagates outward and reaches the borehole interface. The impact force exceeds the dynamic compressive strength of the rock, breaking the rock within 3–4 times the radius of the borehole into fine particles and forming the crush zone. Second, the shock wave attenuates to a stress wave, inducing radial expansion and tangential tensile strain in the rock mass. The cracks then propagate radially along the crush zone, forming the fracture zone, which extends to more than 20 times the radius of the borehole. Finally, the stress wave further attenuates into a blasting seismic wave, which induces only vibrations in the rock mass.

Compared to single-borehole rock blasting without joints, the joint leads to a significant change in dynamic response and rock fracture. Figs. 11–13 give the simulation results of rock blasting with a joint at three borehole-joint distances ($d$ = 25 cm, 50 cm, 100 cm). Each figure presents a comprehensive overview of the rock blasting process, consisting of eight subfigures. The subfigure is divided into two parts: the upper section illustrates the propagation of the blasting stress wave, while the lower section depicts the development of the rock fracture. The title beneath each subfigure corresponds to the respective time point of the observation. These time-based observations help to visualize the progression of the rock blasting with the joint.

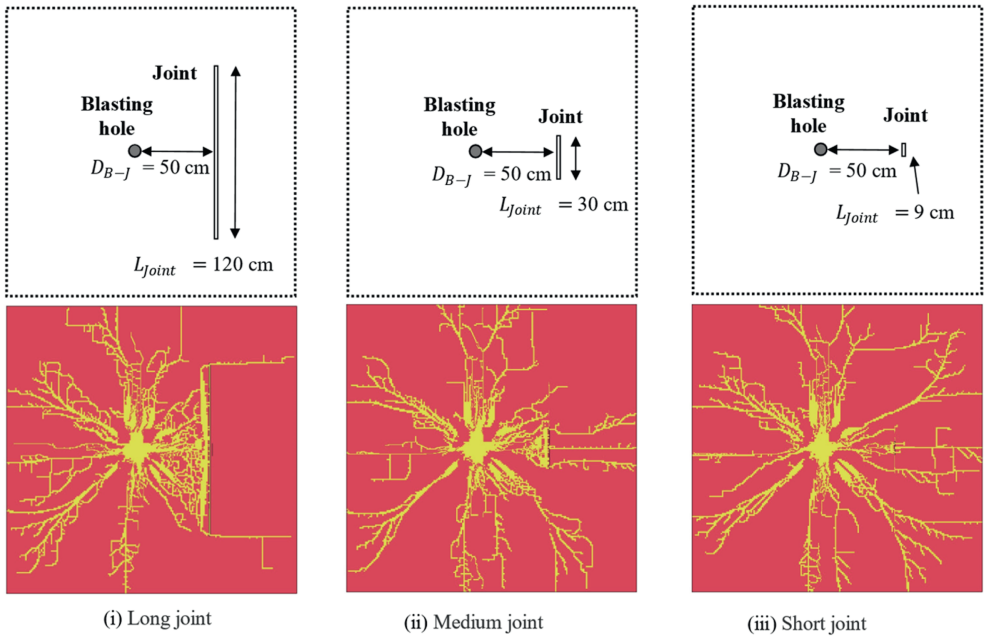
As shown in Fig. 11, the distance $d$ between the borehole and the joint is 25 cm. After detonation, the upper section shows the shock wave generated by the explosion propagating radially outward, which induced the crush zone with a diameter was 18 cm, as shown in the lower section. At 0.07 ms, the blasting stress wave encountered the joint interface and then reflected, while some cracks developed radially around the crush zone. At 0.14 ms, the stress wave propagated outward and reflected continuously, and some cracks began to develop between the borehole and the joint interface, forming a triangular-shaped area with dense cracks. The reflected blasting stress wave induced the tensile strain in the rock mass, altering the distribution of the cracks in the fracture zone. This triangular-shaped region, caused by the reflected stress wave (RSW), is defined as the RSW fracture zone. At 0.22 ms, the stress wave propagated at the tips of the joint and diffracted, which induced the wing cracks, and the RSW fracture zone was highly fragmented. At 0.26 ms, a part of the stress wave was transmitted through the joint and induced cracks behind the joint.

In contrast to single-borehole rock blasting without joints, the final rock fracture mode was divided into four parts: the crushed zone, the fracture zone, the RSW fracture zone, and the fracture zone behind the joint.

When the borehole-joint distance is 50 cm, the influence of the joint on the propagation of the stress wave is much clearer, as shown in Fig. 12. At 0.15 ms, the stress wave just reached the joint interface, and before this, the rock cracks propagated radially,




(a) Three incident angles of blasting stress waves at joint interface




(b) Three different joint lengths

**Fig. 8.** The influence of the incident angle of the blasting stress wave at the joint interface and the joint length on the result. Note: The joint length ($L_{\text{Joint}}$), the angle between the blasting stress wave and the joint direction ($\theta$), the distance from the borehole to the joint tip ($D_{\text{Jtip}}$), and the distance from the borehole to the joint ($D_{\text{B-J}}$) are labeled.

forming the crush zone and the fracture zone. At 0.18 ms, a noticeable stress wave reflection was observed, inducing tensile cracks along the joint interface outside the fracture zone. As the stress wave continued to propagate, these tensile cracks connected with the cracks in the fracture zone, forming the RSW fracture zone at 0.26 ms. The RSW fracture zone was relatively fragmented, with no stress waves transmitting through the joint and no cracks forming behind the joint.

When the borehole-joint distance increased to 100 cm, the formation of the RSW fracture zone was relatively late, as shown in Fig. 13. Until 0.32 ms, the stress wave propagated to the joint interface, and the fracture zone had developed much more fully, consuming more blasting energy. As the distance between the borehole and the joint increased, the propagation and superposition of the reflected stress wave could be observed. At 0.4 ms, the reflected waves propagated towards the borehole and induced the tensile cracks, which initially extended along the joint interface and then formed several layer cracks parallel to the joint. At 0.48 ms, the layer cracks connected with the radial cracks in the fracture zone, promoting the formation of the RSW fracture zone. After the RSW fracture zone was formed, newly generated cracks concentrated in it.

Comparing three simulation results, the borehole-joint distance affects the formation time and fragmentation state of the

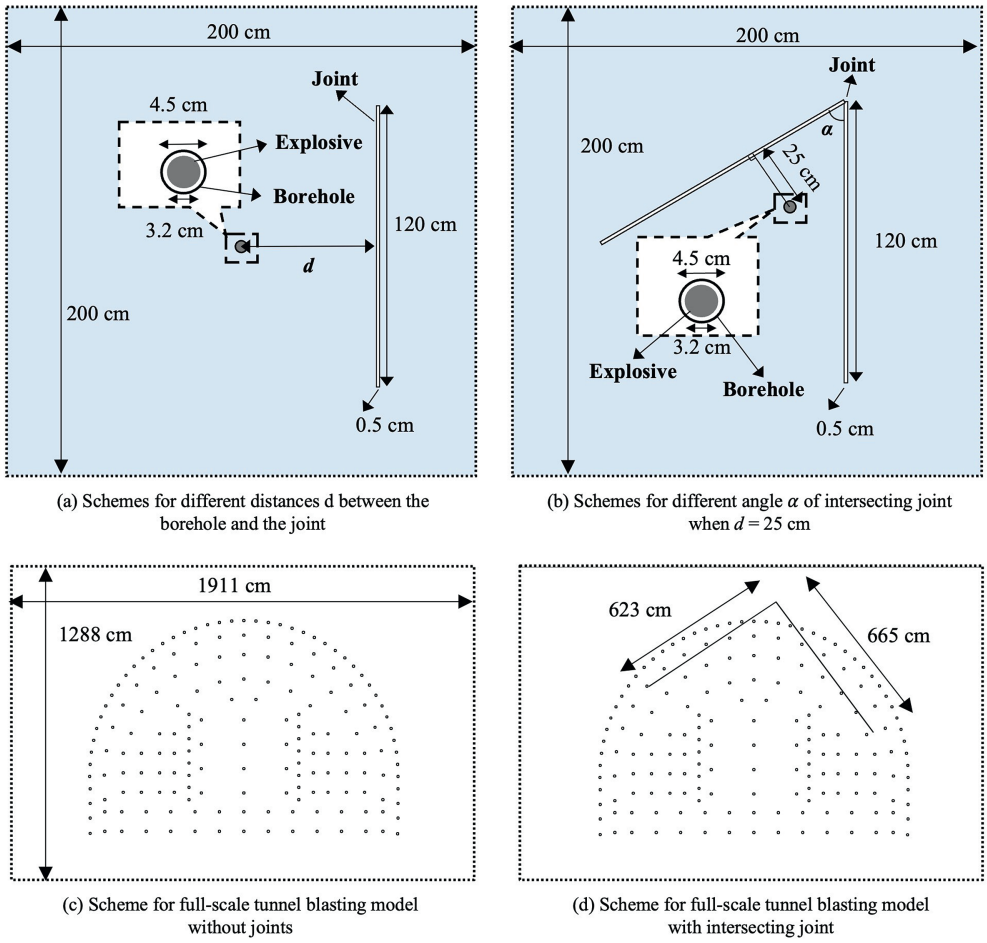



**Fig. 9.** Schematic diagram of the charge, borehole, and joint within the rock.

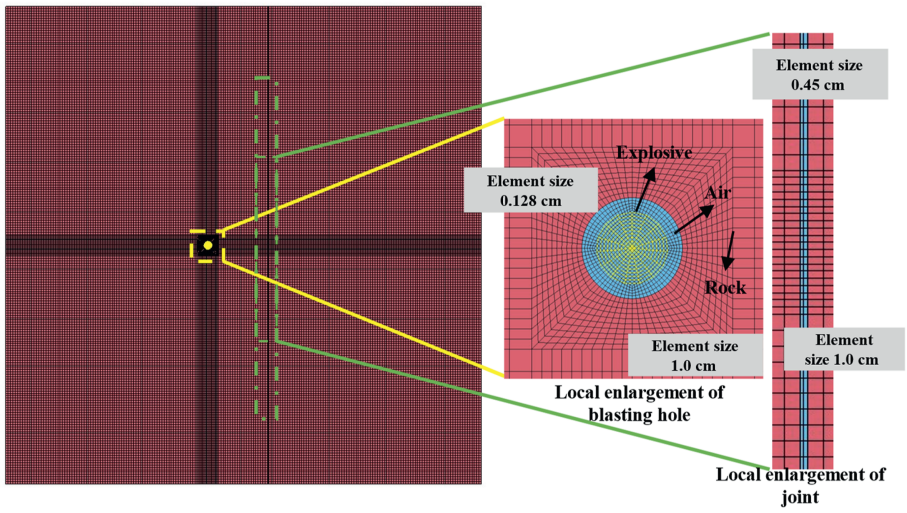



**Fig. 10.** The dynamic finite element model with the local enlargement of the borehole and the joint.

RSW fracture zone, thereby influencing the rock fracture mode. When the distance is short ($d$ = 25 cm), the RSW fracture zone forms rapidly, leading to significant fragmentation in this area, which nearly merges with the crush zone. The rock mass between the borehole and the joint becomes highly fragmented, creating conditions for the generation of transmitted waves. These two zones dissipate a significant amount of explosive wave energy, restricting the development of the fracture zone and resulting in the smallest fracture zone. At a moderate distance ($d$ = 50 cm), the RSW fracture zone forms slightly later, allowing more time for the fracture zone to develop. The cracks in the fracture zone then interconnect with the reflected cracks to form the RSW fracture

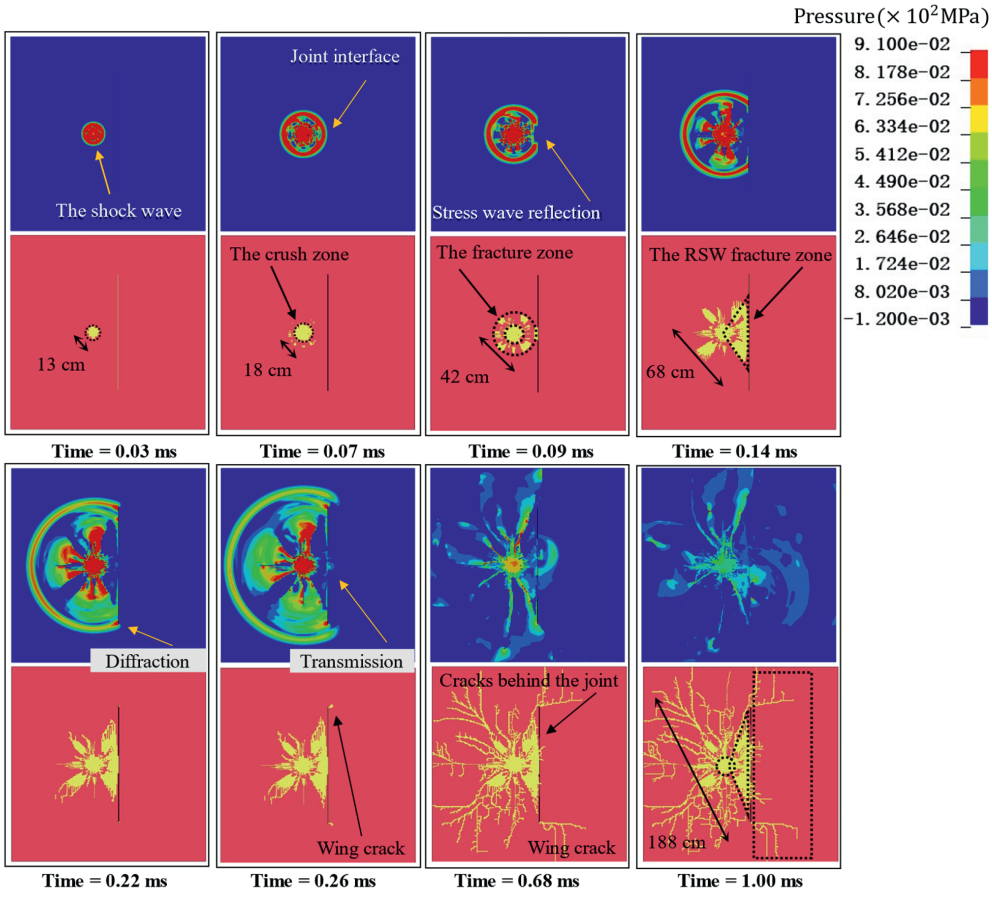



**Fig. 11.** The propagation of the blasting stress wave and the process of the rock fracture at $d = 25$ cm.

zone. The rock mass in this area is relatively fragmented, but no extensive damage occurs. When the distance is large ($d = 100$ cm), the RSW fracture zone forms even later, and the fracture zone has sufficient time to develop fully. As a result, the RSW fracture zone shows the lowest degree of fragmentation, while the fracture zone area is the largest, with a diameter of 212 cm.

In conclusion, the existence of the joint changes the propagation of the blasting stress wave, with most of the wave reflected and inducing tensile cracks, which form the RSW fracture zone. The formation time and the fragmentation state of the RSW fracture zone significantly influence the final rock fracture mode, which is determined by the borehole-joint distance. Once the RSW fracture zone is formed, new cracks tend to preferentially develop within this region, and the rock mass tends to be broken along the RSW fracture zone. For a single joint around the borehole, the profile of the RSW fracture zone is triangular.

### 5.2. Influence of intersecting joint angle

Intersecting joints have a different impact on rock blasting compared to a single joint. The dynamic response and rock fracture process under three intersecting joint angles ($\alpha = 30°$, 60°, and 120°) are shown separately in Figs. 14–16. The borehole is positioned within the intersecting joints, 25 cm from each of the two joints.

Contrary to a single joint within the rock mass, the blasting stress wave was reflected at three points when it propagated to the joint interface: two perpendicular feet from the borehole center to the intersection joints and the crossing point of the intersection joints. Within the interior angle of the intersecting joint, tensile cracks formed at the three reflection positions, and the reflected stress wave continued to propagate and overlap, further accelerating the crack extension. Those tensile cracks formed the RSW fracture zone, which was a quadrangle and resembled the combination of two triangles, like the shape of the RSW fracture zones seen in single-joint simulations. When the RSW fracture zone was significantly fragmented, a portion of the blasting stress wave transmitted through the joint interface, but no significant cracks formed behind the joint surface. Finally, the rock fracture mode was still divided into four zones: the crushed zone, the fracture zone, the RSW fracture zone, and the fracture zone out of the intersecting joint. The RSW fracture zone, which encompassed the crush zone, concentrated most of the cracks.

To quantitatively analyze the rock fragmentation, the degree of the rock fracture was estimated by calculating the ratio of the crack pixels to the total number of pixels, as shown in Table 5.

Several interesting phenomena can be observed:

The presence of joints, especially intersecting joints or those located close to the borehole, causes the rock mass to fracture along the contour of the RSW fracture zone. The degree of rock fracture in the RSW fracture zone was significantly higher than that in the whole rock mass sample. When intersecting joints were present, or when the joints were positioned close to the borehole ($d = 25$ cm), the fracture degree in the RSW fracture zone reached approximately 70 %, more than five times that of the whole rock mass sample. This indicates the rock mass is more likely to fracture along the RSW fracture zone.

As the angle between intersecting joints decreases, the effect

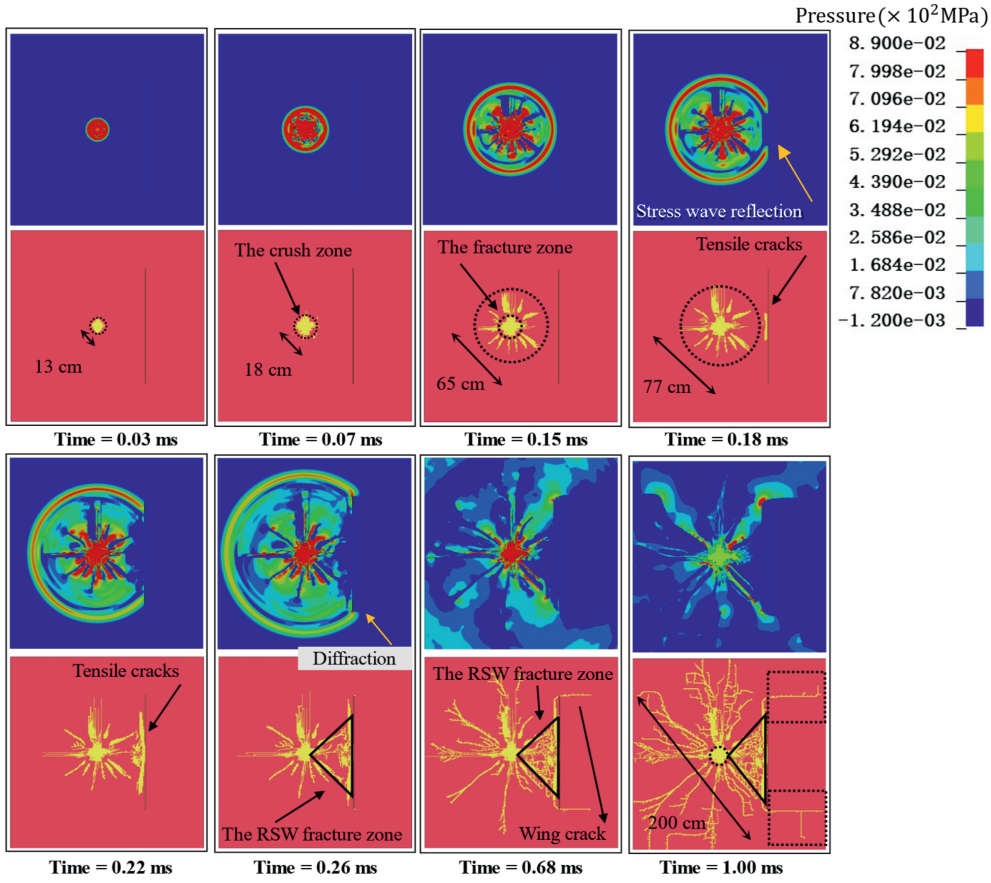



**Fig. 12.** The propagation of the blasting stress wave and the process of the rock fracture at $d = 50$ cm.

on the rock fracture profile becomes more pronounced. To normalize the area, the area of the RSW fracture zone was divided by the total area. As the angle decreased, the area of the RSW fracture zone increased, and when the intersecting joint was an acute angle ($\alpha = 60°$), the possible breaking area of rock mass (i.e. the RSW fracture zone) was the largest, nearly twice that of the other conditions.

The existence of joints, particularly intersecting joints, inhibits the overall crack propagation in the rock. A line chart was created to represent the degree of the rock fracture under various numerical simulation conditions, as illustrated in Fig. 17. The red line represents the whole rock sample, and the blue line represents the RSW fracture zone. The trends of the red line and the blue line are opposite. As the degree of rock fracture in the RSW fracture zone increased, the overall degree of rock fracture decreased. It is inferred that the reflected stress waves induced by the joints propagate within the RSW fracture zone, dissipating blasting energy, which suppresses crack development in other regions, leading to lower overall rock damage.

### 5.3. Field case analysis and validation

During tunnel excavation, the impact of multiple blasting hole coupling, detonation delay time, and hole spacing on the rock fracture must be considered. The full-scale tunnel blasting model is built to simulate the actual conditions of tunnel excavation using the drilling and blasting method. The simulation results are compared with the field measurements to validate the effectiveness of the DFEM method and the reliability of the conclusions.

The sections in the Yinggelin Tunnel at ZK11 + 837.2, ZK11 + 833.3, and ZK11 + 824.8 were penetrated by a set of structural planes, as illustrated in Fig. 18. Fig. 18a shows the restructured tunnel faces with structural planes from the side view and plan view. Fig. 18b gives the line diagram to illustrate the relationship between the joints and the excavation profile more clearly.

The full-scale tunnel excavation model with joints was built according to the overbreak section at ZK11 + 824.8, as shown in Fig. 9d. Fig. 19b, i-iii shows that the stress waves induced by the blasting holes around the joint were reflected and transmitted at the joint interface. The overlapping blasting-induced stress waves changed the propagation direction at the intersection of the joints. Compared with the results of the tunnel excavation model without joints, as shown in Fig. 19a, an overbreak occurred at the position of the intersecting joint, forming a rock fracture area along the joint edge (i.e. the RSW fracture zone profile).

The field measurement results, as shown in Figs. 18 and 20b, i, showed that the rock area within the intersecting joint was fractured along the joint edges. When the intersecting joint was located outside the contour boreholes, the triangle-shaped overbreak occurred, which was consistent with the numerical simulation results.

The Hausdorff distance was used to quantitatively evaluate the similarity between the tunnel blasting profiles from the numerical simulation and the field measurement. It is defined as the maximum distance from any point in one graph to its nearest point in the other graph. A smaller Hausdorff distance indicates greater geometric similarity between the two graphics.

A tunnel excavation profile slice was extracted from the reconstructed point cloud model, as shown in Fig. 20b, ii. The rock

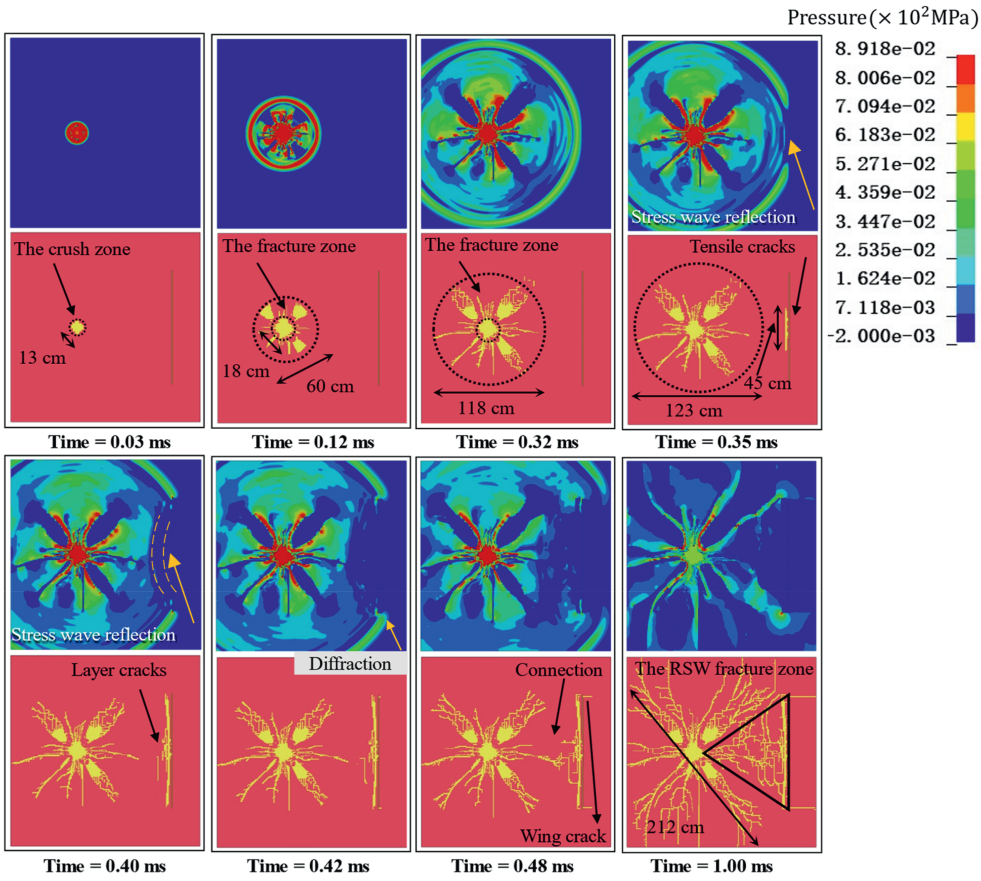



**Fig. 13.** The propagation of the blasting stress wave and the process of the rock fracture at $d = 100$ cm.

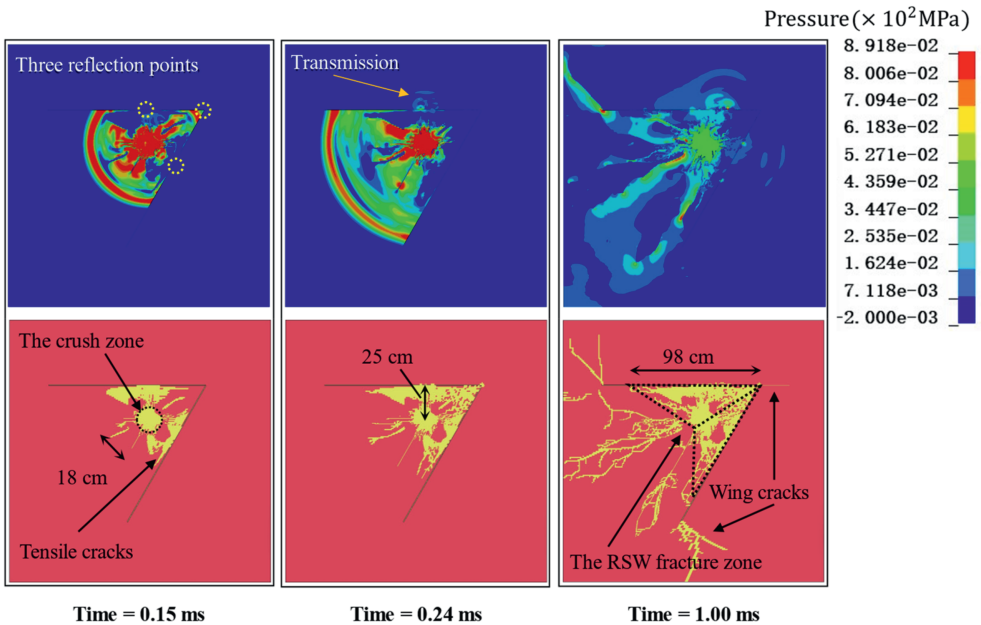



**Fig. 14.** The propagation of the explosive stress wave and the process of the rock fracture at the angle of $\alpha = 60°$.

fracture area from the numerical simulation was identified using color coding, and the fracture features were enhanced through the mask image shown in Fig. 20a, i. The rock fracture contour from the numerical simulation is the maximum outer profile of the mask image, as indicated in Fig. 20a, ii. To minimize potential errors caused by the low-density points in the lower region of the tunnel face model, the contour is divided into upper and lower portions for separate comparison, shown in Fig. 20a, iii and b, iii.

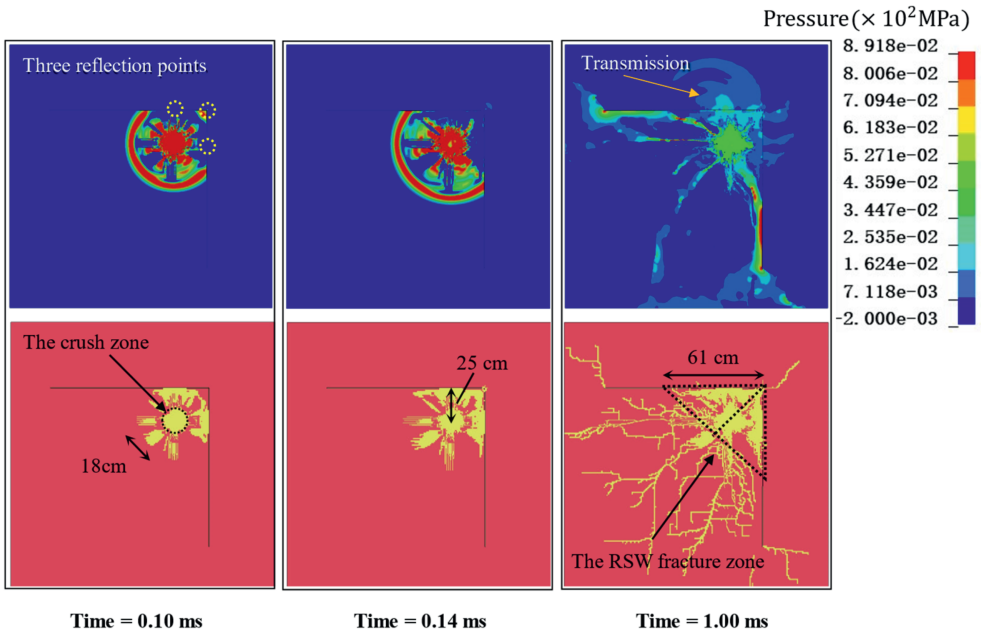



**Fig. 15.** The propagation of the explosive stress wave and the process of the rock fracture at the angle of $\alpha = 90°$.

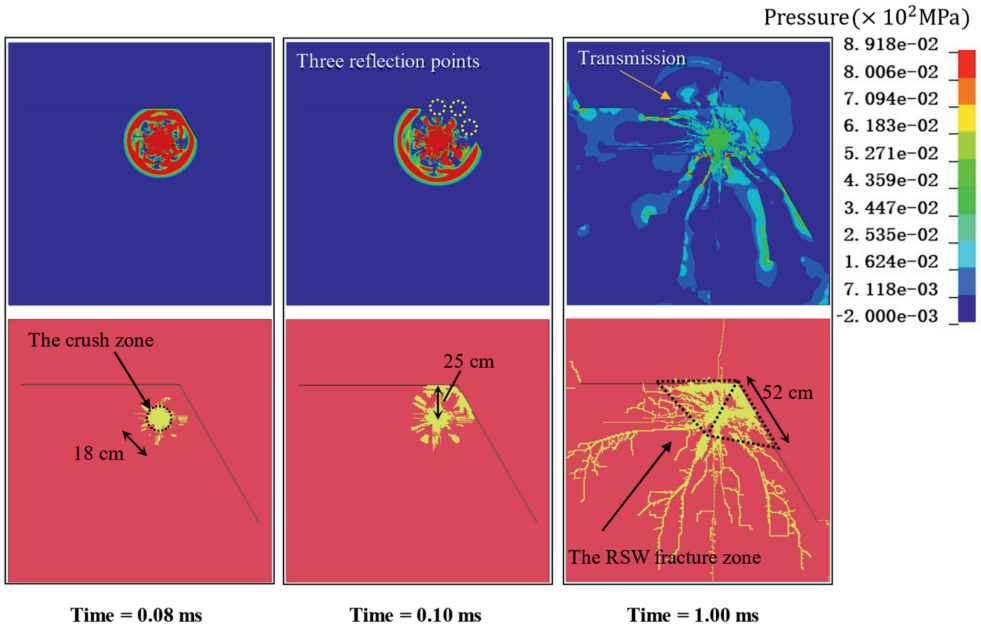



**Fig. 16.** The propagation of the explosive stress wave and the process of the rock fracture at the angle of $\alpha = 120°$.

**Table 5**
The degree of rock fragmentation under different experimental conditions.

| Condition | Degree of rock fracture of the whole rock mass sample | Degree of rock fracture in the RSW fracture zone | Normalized area of the RSW fracture zone |
|---|---|---|---|
| $\alpha = 60°$ | 7.8 % | 68.1 % | 0.061 |
| $\alpha = 90°$ | 9 % | 74.7 % | 0.038 |
| $\alpha = 120°$ | 8.8 % | 72.1 % | 0.033 |
| $d = 25$ cm | 13.7 % | 70.5 % | 0.038 |
| $d = 50$ cm | 13.6 % | 47.4 % | 0.053 |
| $d = 100$ cm | 15.4 % | 25 % | 0.125 |

Note: $\alpha$ is the intersecting joint angle; $d$ is the borehole-joint distance.

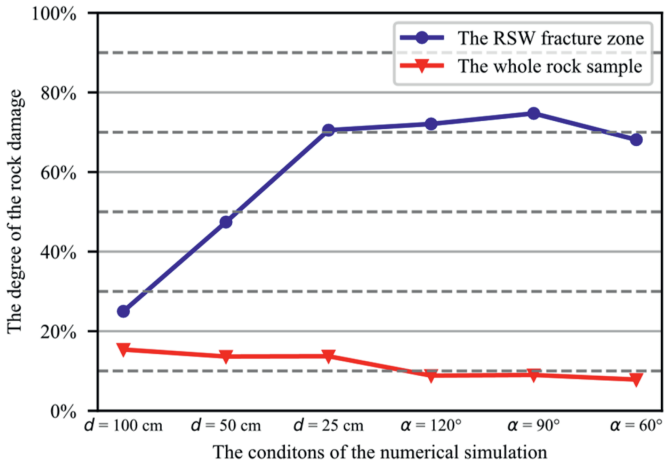



**Fig. 17.** Line chart of rock fracture degree under various numerical simulation conditions.

The normalized Hausdorff distance between the upper portions of the two profiles is 0.0494, indicating a high degree of similarity. The consistency between the numerical simulation results and field measurements validates the effectiveness and reliability of the numerical method.

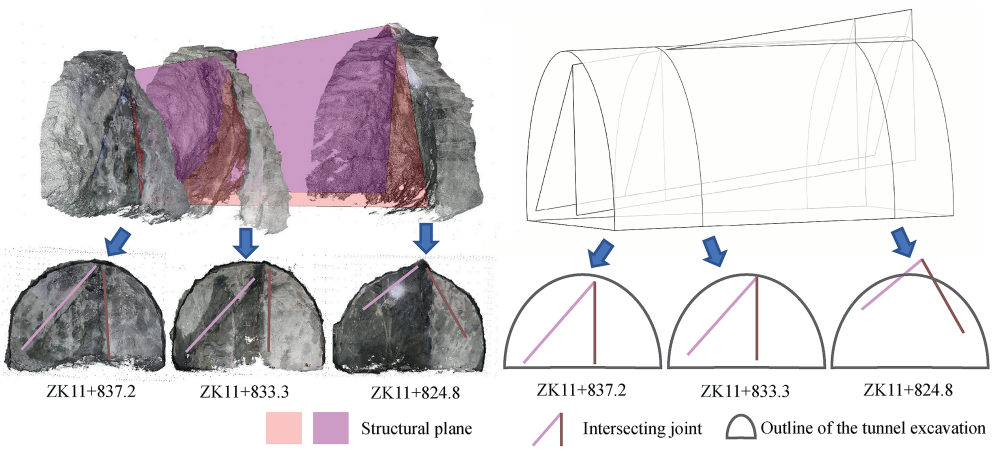
According to the results, the presence of significant joints, particularly intersecting joints near the outside of the contour boreholes, promotes the rock fracture along the RSW fracture zone profile, which raises the probability of triangle-shaped overbreak.

## 6. Conclusions

This study analyzed the influence of joint distribution in hard rock mass on the tunnel blasting profile. Through the real-time field measurement of the tunnel face using the digital twin method, it was observed that when the properties of the hard rock mass and the blasting design remained unchanged, the overbreak occasionally occurred in certain sections of the tunnel. The boundary of the overbreak aligned with the joint distribution. It was reasoned that the joint distribution has a significant effect on the tunnel blasting profile in the hard rock mass. The dynamic finite element method is used to investigate the influence of borehole-joint distance and the intersecting joint angle on the dynamic response and the damage mechanisms of the hard rock mass. The numerical simulation results showed that joints have both guiding and restraining effects on the propagation of blasting stress waves and the development of fractures in the hard rock mass. Furthermore, the simulation results closely matched the field observations. The specific conclusions are as follows:

(1) The existence of joints within the hard rock mass has changed the propagation path of the blasting stress waves. The majority of the blasting stress waves reflect when they propagate to the joint interface and cause the rock mass to crack. A minority of them diffract at the joint tips and introduce the wing crack in the rock. When the rock between the borehole and the joint is relatively fragmented, a few of the blasting stress waves transmit through and cause the rock mass to crack behind the discontinuity.
(2) The existence of the joint has also changed the rock-blasting fracture mode, which divides the rock failure into four regions, with the two additional regions being the RSW fracture zone and the fracture zone behind the joint (i.e. the wing cracks and the transmitted wave cracks). Once the RSW fracture zone is formed, the cracks mainly develop in it, making the rock mass more prone to fracture along the RSW fracture zone.
(3) The borehole-joint distance and the intersecting joint angle influence the area and fracture degree of the RSW fracture zone. The fracture degree increases as the joint approaches the borehole, and the area expands as the intersecting joint angle decreases.
(4) In tunnel construction, when joints, especially intersecting joints, are located near the outer region of the contour boreholes, the rock mass tends to fracture according to the profile of the RSW fracture zone, which increases the likelihood of triangle-shaped overbreak.

However, several limitations should be noted. First, the study did not fully consider the complex 3D spatial relationship between structural planes and blasting holes. The angle between the stress wave propagation direction and the structural planes plays a significant role in blasting performance, yet only 2D simulations were conducted due to computational limitations. Second, the analysis was restricted to open joints, excluding the influence of infilled joints due to a lack of reliable material data. Third, the




(a) Restructured tunnel faces using digital twin method (b) Line diagram of the tunnel and the joints

**Fig. 18.** The spatial relationship between the structural plane and the tunnel face.

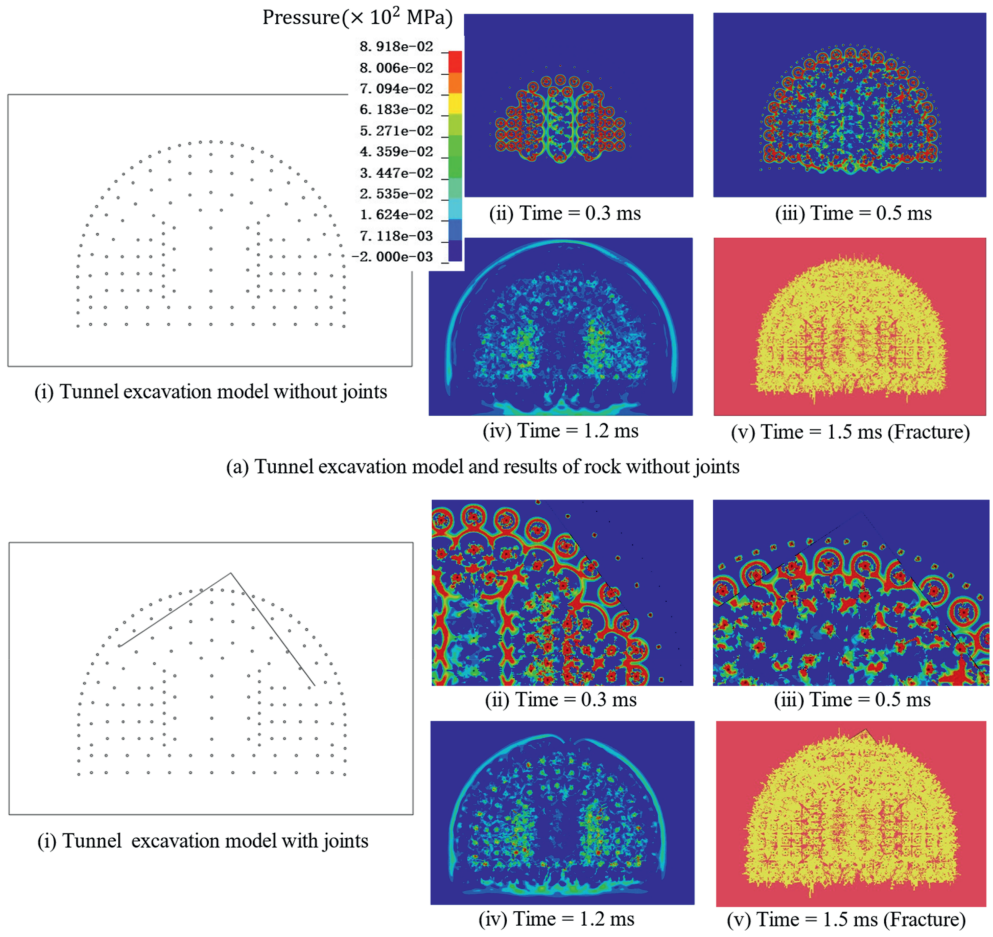



**Fig. 19.** Numerical simulation results of tunnel blasting in the rock mass with and without significant joints at ZK11 + 824.8.

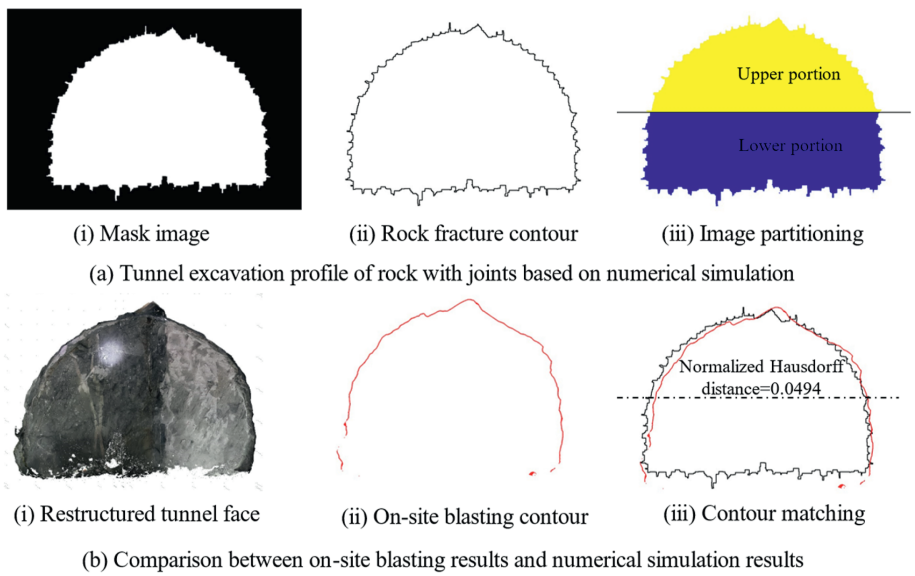



**Fig. 20.** Similarity analysis of numerical simulation and on-site tunnel excavation profiles at ZK11 + 824.8.

optimization of blasting parameters—such as blast hole placement, spacing, charge structure, and delay timing—in jointed rock masses remains to be studied.

Future studies should consider the 3D spatial distribution of joints and structural planes to provide a more comprehensive understanding of their effects on tunnel blasting excavation. Moreover, investigating different joint types and their mechanical behaviors under blasting loads to improve excavation accuracy and reduce the joint-induced overbreak.

## CRediT authorship contribution statement

**Junxin Li:** Writing – original draft, Investigation, Visualization, Software, Methodology. **Wei Wu:** Conceptualization, Writing – review & editing, Funding acquisition. **Bingyi Pan:** Software, Visualization, Data curation. **Baosheng Dong:** Resources, Project administration. **Hehua Zhu:** Funding acquisition, Supervision, Conceptualization.

## Declaration of generative AI and AI-assisted technologies in the writing process

During the preparation of this work, the authors used ChatGPT to refine and enhance the clarity of the academic writing. After using this tool, the authors reviewed and edited the content as needed and take full responsibility for the content of the publication.

## Declaration of competing interest

The authors declare that they have no known competing financial interests or personal relationships that could have appeared to influence the work reported in this paper.

## Acknowledgments

We acknowledge the funding support from the National Natural Science Foundation of China (Grant No. 42272338), the Major Research and Development Projects of China Communications Construction Company (Grant No. 2024-ZJKJ-16), and the Special Project for Performance Incentive and Guidance of Scientific Research Institutions in Chongqing (Grant No. CSTB2023JXJL-YFX0006). The authors also acknowledge the assistance of Dr. Pengfei Yan and Dr. Xi Wang for providing language help and proofreading the article.

## References

Barton, N., Lien, R., Lunde, J., 1974. Engineering classification of rock masses for the design of tunnel support. Rock Mech. 6 (4), 189–236.
Cai, Y., Yan, P., 2024. Three-dimensional partition-of-unity generalized node method for the simulation of fractured rock mass. Comput. Methods Appl. Mech. Eng. 419, 116688.
Chakraborty, A.K., Jethwa, J.L., Paithankar, A.G., 1994. Effects of joint orientation and rock mass quality on tunnel blasting. Eng. Geol. 37 (3), 247–262.
Chen, J., Li, X., Zhu, H., Rubin, Y., 2017. Geostatistical method for inferring RMR ahead of tunnel face excavation using dynamically exposed geological information. Eng. Geol. 228, 214–223.
Dehghan Banadaki, M.M., Mohanty, B., 2012. Numerical simulation of stress wave induced fractures in rock. Int. J. Impact Eng. 40–41, 16–25.
Donea, J., Huerta, A., Ponthot, J.-Ph, Rodríguez-Ferran, A., 2004. Encyclopedia of Computational Mechanics. John Wiley & Sons, Ltd, Chichester, West Sussex, England.
Fang, W., Chen, W., Love, P.E.D., Luo, H., Zhu, H., Liu, J., 2024. A status digital twin approach for physically monitoring over-and-under excavation in large tunnels. Adv. Eng. Inform. 62, 102648.
Fornberg, B., Flyer, N., 2015. Solving PDEs with radial basis functions. Acta. Numer. 24, 215–258.
Holmquist, T.J., Johnson, G.R., Cook, W.H., 1993. A computational constitutive model for concrete subjected to large strains, high strain rates and high pressures - TIB. Bri. Library Conf. Proceed. 2, 591–600. Quebec, Canada.
Hong, Z., Tao, M., Zhao, R., Zhou, J., Zhao, M., 2023. Investigation on overbreak and underbreak of pre-stressed tunnels under the impact of decoupled charge blasting. Int. J. Impact Eng. 182, 104784.
Kumar, P., Mohammadi, H., Chopra, R., Kumar Tyagi, S., Kumar Pandey, S., 2023. A newly developed blasting cut in tunnels; application of "combined method" in small to medium-sized tunnels. Tunn. Undergr. Space Technol. 142, 105426.
Li, C., Yang, R., Zuo, J., Xie, P., 2025. Theory and field tests of innovative cut blasting method for rock roadway excavation. Tunn. Undergr. Space Technol. 155, 106180.
Li, X., Chen, Z., Chen, J., Zhu, H., 2019. Automatic characterization of rock mass discontinuities using 3D point clouds. Eng. Geol. 259, 105131.
Liang, X., Ding, C., Zhu, X., Zhou, J., Chen, C., Guo, X., 2024. Visualization study on stress evolution and crack propagation of jointed rock mass under blasting load. Eng. Fract. Mech. 296, 109833.
Ling, T., Li, S., Liu, D., Liang, S., 2023. Blasting damage of tunnel rock mass based on cumulative effect. Rock Mech. Rock Eng. 56 (3), 1679–1695.
Lisjak, A., Grasselli, G., 2014. A review of discrete modeling techniques for fracturing processes in discontinuous rock masses. J. Rock Mech. Geotech. Eng. 6 (4), 301–314.
Liu, W.K., Li, S., Park, H.S., 2022. Eighty years of the finite element method: birth, evolution, and future. Arch. Comput. Methods Eng. 29 (6), 4431–4453.
Lyu, G., Zhou, C., Jiang, N., 2023. Experimental and numerical study on tunnel blasting induced damage characteristics of grouted surrounding rock in fault zones. Rock Mech. Rock Eng. 56 (1), 603–617.
Ma, G.W., An, X.M., 2008. Numerical simulation of blasting-induced rock fractures. Int. J. Rock Mech. Min. Sci. 45 (6), 966–975.
Ma, J., Zhao, J., Lin, Y., et al., 2023. Study on tamped spherical detonation-induced dynamic responses of rock and PMMA through mini-chemical explosion tests and a four-dimensional lattice spring model. Rock Mech. Rock Eng. 56 (10), 7357–7375.
Menikoff, R., 2015. JWL Equation of State. Los Alamos National Laboratory. New Mexico, United States.
Potyondy, D.O., Cundall, P.A., 2004. A bonded-particle model for rock. Int. J. Rock Mech. Min. Sci. 41 (8), 1329–1364.
Qin, C., Ma, C., Li, L., Sun, X., Liu, Z., Sun, Z., 2023. Development and application of an intelligent robot for rock mass structure detection: a case study of Letuan tunnel in Shandong, China. Int. J. Rock Mech. Min. Sci. 169, 105419.
Saadatmand Hashemi, A., Katsabanis, P., 2020. The effect of stress wave interaction and delay timing on blast-induced rock damage and fragmentation. Rock Mech. Rock Eng. 53 (5), 2327–2346.
Sanchidrián, J.A., Segarra, P., Ouchterlony, F., Gómez, S., 2022. The influential role of powder factor vs. Delay in full-scale blasting: a perspective through the fragment size-energy fan. Rock Mech. Rock Eng. 55 (7), 4209–4236.
Singh, S.P., Xavier, P., 2005. Causes, impact and control of overbreak in underground excavations. Tunn. Undergr. Space Technol. 20 (1), 63–71.
Tahir, Y., Kadiri, I., Fertahi, S.E., et al., 2023. Design of controlled pre-split blasting in a hydroelectric construction project. Civ. Eng, J.-Tehran 9 (3), 556–566.
Tawadrous, A., 2011. Hard Rocks under High Strain-Rate Loading. Queen's University, Ontario, CA, Canada. PhD Thesis.
Tian, Y., Chen, W., Tian, H., Shu, X., He, L., Huang, M., 2024. Physical model test and application of 3D printing rock-like specimens to laminated rock tunnels. J. Rock Mech. Geotech. Eng. 16 (11), 4625–4637.
Vazaios, I., Vlachopoulos, N., Diederichs, M.S., 2019. Assessing fracturing mechanisms and evolution of excavation damaged zone of tunnels in interlocked rock masses at high stresses using a finite-discrete element approach. J. Rock Mech. Geotech. Eng. 11 (4), 701–722.
Wang, D., Bienen, B., Nazem, M., et al., 2015. Large deformation finite element analyses in geotechnical engineering. Comput. Geotech. 65, 104–114.
Wang, X., Li, J., Zhao, X., Liang, Y., 2022. Propagation characteristics and prediction of blast-induced vibration on closely spaced rock tunnels. Tunn. Undergr. Space Technol. 123, 104416.
Wang, X., Yin, Z.-Y., 2025. Physics-encoded convolutional attention network for forward and inverse analysis of spatial-temporal parabolic dynamics considering discontinuous heterogeneity. Comput. Methods Appl. Mech. Eng. 442, 118025.
Wang, X., Yin, Z.-Y., Wu, W., Zhu, H.-H., 2025. Differentiable finite element method with Galerkin discretization for fast and accurate inverse analysis of multidimensional heterogeneous engineering structures. Comput. Methods Appl. Mech. Eng. 437, 117755.
Wang, Y., Luo, L., Wang, Z., Kong, W., Yang, R., 2024. 3D damage and failure patterns in rock due to blasting at different open joints dig angles. Rock Mech. Rock Eng.
Wen, L., Li, X., Wu, Q., Su, W., 2016. Study on parameters of Holmquist-Johnson-Cook model for granite porphyry. Chin. J. Comput. Mech. 33 (5), 725–731 (in Chinese).
Wu, H., Gong, M., Yang, R., Wu, X., Liu, X., 2023. Double-face intelligent hole position planning method for precision blasting in roadways using a computer-controlled drill jumbo. Int. J. Miner. Metall. Mater. 30 (6), 1025–1037.
Xue, Y., Cao, Y., Zhou, M., Zhang, F., Shen, K., Jia, F., 2023. Rock mass fracture maps prediction based on spatiotemporal image sequence modeling. Comput. Aided Civ. Infrastruct. Eng. 38 (4), 470–488.
Yang, R., Wang, Y., Ding, C., 2016. Laboratory study of wave propagation due to explosion in a jointed medium. Int. J. Rock Mech. Min. Sci. 81, 70–78.
Yao, S., Zhang, D., Lu, F., Chen, X., Zhao, P., 2017. A combined experimental and numerical investigation on the scaling laws for steel box structures subjected

to internal blast loading. Int. J. Impact Eng. 102, 36–46.
Ye, Z., Ye, Y., Zhang, C., et al., 2023. A digital twin approach for tunnel construction safety early warning and management. Comput. Ind. 144, 103783.
Zhang, K., Wu, W., Liu, Y., Xie, T., Zhou, J., Zhu, H., 2024. OCFMD: an automatic optimal clustering method of discontinuity orientation based on Fisher mixed distribution. Rock Mech. Rock Eng. 57 (3), 1735–1763.
Zhang, K., Wu, W., Zhu, H., Zhang, L., Li, X., Zhang, H., 2020. A modified method of discontinuity trace mapping using three-dimensional point clouds of rock mass surfaces. J. Rock Mech. Geotech. Eng. 12 (3), 571–586.
Zhang, Q., He, M., Wang, J., et al., 2022. Investigation of a non-explosive directional roof cutting technology for self-formed roadway. Int. J. Min. Sci. Technol. 32 (5), 997–1008.
Zhang, Z.-X., Sanchidrián, J.A., Ouchterlony, F., Luukkanen, S., 2023. Reduction of fragment size from mining to mineral processing: a review. Rock Mech. Rock Eng. 56 (1), 747–778.
Zhu, Hehua, Wu, Wei, Xiaojun, Li, Chen, Jianqin, Huang, Xianbin, 2017. High-precision acquisition, analysis and service of rock tunnel information based on iS3 platform. Chin. J. Rock Mech. Eng. 36 (10), 2350–2364 (in Chinese).
Zhu, Z., Mohanty, B., Xie, H., 2007. Numerical investigation of blasting-induced crack initiation and propagation in rocks. Int. J. Rock Mech. Min. Sci. 44 (3), 412–424.
Zou, D., 2017a. Blasting design for underground excavation. In: Zou, D. (Ed.), Theory and Technology of Rock Excavation for Civil Engineering. Springer, Singapore, pp. 509–551.
Zou, D., 2017b. Introduction to underground excavation by drilling and blasting. In: Zou, D. (Ed.), Theory and Technology of Rock Excavation for Civil Engineering. Springer, Singapore, pp. 483–502.
Zuazua, E., 2005. Propagation, observation, and control of waves approximated by finite difference methods. SIAM Rev. 47 (2), 197–243.



**Junxin Li** is a PhD candidate in Civil Engineering at Tongji University, Shanghai, China, under the supervision of Prof. Hehua Zhu. She obtained her BSc degree in Civil Engineering from Beijing Jiaotong University, Beijing, China, in 2020. Her research interests include: (1) Numerical simulation and analysis of geotechnical and rock engineering, and (2) The mechanisms, monitoring, and prediction of adverse geological conditions during tunnel excavation.